Earth Syst. Sci. Data Discuss., 8, 509–566, 2015
www.earth-syst-sci-data-discuss.net/8/509/2015/
doi:10.5194/essdd-8-509-2015

Open Access Earth System Science Data Discussions

Objective mapping of Argo data in the Weddell Gyre: a gridded dataset of upper ocean water properties

K. A. Reeve[1], **O. Boebel**[1], **T. Kanzow**[1], **V. Strass**[1], **G. Rohardt**[1], **and E. Fahrbach**[1,†]

[1]Alfred-Wegener-Institut for Polar and Marine Research, Bremerhaven, Germany
[†]deceased

Received: 3 March 2015 – Accepted: 29 May 2015 – Published: 23 June 2015

Correspondence to: K. A. Reeve (krissy.reeve@awi.de)

Published by Copernicus Publications.

Abstract

The Weddell Gyre plays a crucial role in the modification of climate by advecting heat poleward to the Antarctic ice shelves and by regulating the density of water masses that feed the lowest limb of the global ocean overturning circulation. However, our understanding of Weddell Gyre water mass properties is limited to regions of data availability, primarily along the Prime Meridian. The aim of this paper is to provide a dataset of the upper water column properties of the entire Weddell Gyre. Objective mapping was applied to Argo float data in order to produce spatially gridded, time composite maps of temperature and salinity for fixed pressure levels ranging from 50 to 2000 dbar, as well as temperature, salinity and pressure at the level of the subsurface temperature maximum. While the data are currently too limited to incorporate time into the gridded structure, the data are extensive enough to produce maps of the entire region across three time composite periods (2002–2005, 2006–2009 and 2010–2013), which can be used to determine how representative conclusions drawn from data collected along general *RV* transect lines are on a gyre scale perspective. The work presented here represents the technical prerequisite in addressing climatological research questions in forthcoming studies. These data sets are available in netCDF format at doi:10.1594/PANGAEA.842876.

1 Introduction

The Weddell Gyre provides an important link between the upper ocean and the ocean interior through the formation of Weddell Sea Deep Water (WSDW) and Weddell Sea Bottom Water (WSBW). WSDW in particular contributes significantly to Antarctic Bottom Water; a prominent water mass present throughout much of the abyssal global ocean (Orsi et al., 1999; Johnson, 2008). As such, the Weddell Gyre acts as a buffer through its role in transferring heat into the deep ocean; potentially playing a key role in a changing climate (Fahrbach et al., 2011).

ESSDD
8, 509–566, 2015

The main source water of the Weddell Gyre, Circumpolar Deep Water (CDW), enters at intermediate depths primarily from the east, although the open northern boundary permits intrusions of CDW to a lesser extent (Klatt et al., 2005; Fahrbach et al., 2004, 2011; Cisewski et al., 2011). Upon entering the gyre, CDW becomes known as Warm Deep Water (WDW) and can be identified by its sub-surface potential temperature maximum of 0.6–1 °C (Fahrbach et al., 2011). WDW undergoes water mass transformation to form the underlying water masses. This process is controlled by (1) the transport and mixing of source waters into the gyre (Leach et al., 2011), (2) changes within the Weddell Gyre and on the adjacent shelves by influences from sea-ice and ice-shelves, and finally (3) the transport of modified water masses with the gyre outflow (Foster et al., 1987; Fahrbach et al., 1994, 1995, 2011). A schematic showing the basic Weddell Gyre circulation overlying a map of the bathymetry is shown in Fig. 1.

It has been well documented that the global ocean is warming (Lyman et al., 2010; Levitus et al., 2012; Abraham et al., 2013). Furthermore, observations show a warming trend in the upper parts of the CDW (Boning et al., 2008; Gille, 2008) as well as in AABW within the Atlantic Ocean (Purkey and Johnson, 2013; Couldrey et al., 2013; Azaneu et al., 2013). Within the Weddell Gyre, a general increase in potential temperature of the WSDW and WSBW from the 1980s until 2008 has been observed, along with a warming of the entire water column over 24 years (Fahrbach et al., 2011). It therefore stands to reason that the key water mass that links the above mentioned water masses may also be warming. However, WDW is renowned for being subject to significant variation from year to year (Robertson et al., 2002; Fahrbach et al., 2011), complicating the issue as to whether or not long-term change is occurring.

To date, the literature focusing on Weddell Gyre hydrography has been largely based on observations from repeat hydrographic sections – primarily collected during various cruises (e.g. Fahrbach et al., 2004, 2007, 2011), as well as data from moorings, deployed both along the Prime Meridian and strategically placed locations throughout the gyre (Fahrbach and De Baar, 2010; Klatt et al., 2005; Behrendt et al., 2011). While these data are well-established; there are now 30 years of data collected from *RV Po-*

ESSDD
8, 509–566, 2015

Iarstern alone; the data nevertheless provides only snapshots in time that cover a relatively small region of the Weddell Gyre (Fahrbach et al., 2007). Fahrbach et al. (2011) provides an in-depth comprehensive analysis of the variations within the Weddell System. However, much of the analysis of long-term changes is based on data along the Prime Meridian only – a region of high variability due to its close proximity to Maud Rise – influencing the relatively high frequency fluctuations of observed WDW properties.

In addition to repeat hydrographic sections and moorings throughout the Weddell Gyre, Argo floats have been deployed in the region since 2000. Argo is a global array of over 3500 free-drifting profiling floats that measure the temperature and salinity of the upper 2000 m of the ocean, allowing for continuous monitoring of the global upper ocean. While in the major ocean basins the data are abundant enough to provide a relatively uniform distribution of data throughout, the deployment of Argo floats at high latitudes has been considerably more limited, especially prior to 2007. This is due to the risk of damage to floats resulting from the seasonal presence of sea ice; preventing the float from surfacing or converging around the float while it is at the surface transmitting data to satellite, thus crushing and damaging the float. A sea-ice sensing algorithm was introduced to floats after 2007 (Klatt et al., 2007) whereby floats would "sense" the likelihood of sea-ice at the surface, and may subsequently temporarily abort mission to surface, storing the hydrographic data until the next opportunity to surface arises. The location of the float at (1) the last profile prior to entering the sea-ice zone, and (2) the first profile upon exiting the sea-ice zone, are linearly interpolated in order to provide a rough guess of the float location for the profiles that took place under the sea-ice. Such profiles can be seen in particular in Fig. 2d. There are symbols distributed along straight lines; these represent the linearly interpolated location estimates of stored profile stations while the float is under ice.

There are now over 10 years of Argo float data available for the entire Weddell Gyre region, spanning from December 2001 to present, which can be used to determine the spatial variation of upper water column properties throughout the gyre. However, due to the irregular nature of the free-drifting profiling float, both in a spatial and temporal

ESSDD
8, 509–566, 2015

context, there are significant challenges regarding the utilization of these data in the creation of statistically robust gridded datasets. One common method in dealing with profile data is the application of objective mapping; an adapted form of kriging first developed in application to oceanography by Bretherton et al. (1976), though a similar method was previously applied in a meteorological context (Gandin, 1965). The technique is based on the Gauss–Markov Theorem and provides a point-wise estimate of the interpolated field; this estimate is linear and unbiased and is based on the minimization of the expected interpolation error (i.e. is optimal in the least squares sense; Gandin, 1965; McIntosh, 1990). The method also provides a map of error variance which takes into account the spatial distribution of the data used.

The objective mapping method has been implemented for a number of studies. Wong et al. (2003) and Böhme and Send (2005) have applied the method in a two-stage procedure in order to calibrate float profile salinity data, while Rabe et al. (2011) mapped Arctic observation data in order to determine changes in freshwater content. On a global scale, objective mapping has been used to provide monthly hydrographic fields for the World Ocean Atlas (Chang et al., 2009) and to determine warming of the global upper ocean (Lyman et al., 2010; Lyman and Johnson, 2008). The dynamic nature of the major ocean basins and the relatively sensitive salinity investigations require temporally and spatially dense data in order to apply objective mapping at suitable spatial and temporal correlation length scales. The studies described above were feasible as there is a significantly higher volume of data available for the lower and intermediate latitudes of the ocean than at high latitudes. However, the limited volume of data at high latitudes is such that when objective mapping has been applied to float data on a global scale, regions south of ~ 50–60° S are poorly represented in the mapping process and are typically the primary cause of discrepancies (e.g. Roemmich and Gilson, 2009; von Schuckmann and Le Traon, 2011; Chang et al., 2009).

The aim of this paper is to provide a spatially gridded dataset of the upper water column properties with particular focus on the entire Weddell Gyre. We describe the method followed in order to objectively map the irregular Argo float profile data

ESSDD
8, 509–566, 2015

onto regularly gridded fields, excluding regions beyond the Weddell Gyre boundaries. Associated mapping errors are also provided. While spatially gridded, the resulting mapped fields represent time composites of three separate time periods (2002–2005, 2006–2009 and 2010–2013), since the data are currently too limited to incorporate both a spatial and temporal averaging scheme.

2 Methods

2.1 Data: pre-mapping processing

Float profile data was retrieved from the Coriolis website (www.coriolis.eu.org). All profiles from within the Weddell Gyre region (50 to 80° S; 70° W to 40° E) from December 2001 to March 2013 were selected. While there are 25 848 profiles, only profiles that have been subjected to delayed-mode quality control processing are used in this study, which leaves about 19 600. The profiles are checked for duplicates which are subsequently removed. The majority of available delayed-mode profiles occur in 2008 and 2009 (Fig. 3). While there is a clear seasonal bias in the number of profiles in the first half of the time series, this bias reduces after 2007. This is due to the introduction of an ice-sensing algorithm that allows floats to abort the present mission to surface if the presence of sea-ice is predicted at the surface (Klatt et al., 2007; Fig. 3). The majority of profiles have a vertical limit of 2000 dbar, although there are more than 1500 profiles that are limited to 1000 dbar (about 75 % of these profiles are actually located north of the gyre boundary and most likely occur due to the complex bottom bathymetry of the region. Some of these "shallow" profiles within close proximity to Maud Rise may also be explained by bottom bathymetry). Data are filtered according to their corresponding quality flags; only those with a quality flag of 1 are used, which indicates that the data have passed all quality control tests and that the "adjusted value is statistically consistent" (for more information about the quality control procedure of Argo floats, refer to the quality control manual at www.argodatamgt.org). Additionally, any data points

ESSDD
8, 509–566, 2015

where the corresponding adjusted pressure error exceeds 20 dbar are rejected. This is in accordance with the guidelines provided on the Argo website (www.argo.ucsd.edu). The temperatures in Argo are reported to be accurate to ±0.002 °C while pressures are accurate to ±2.4 dbar (Owens and Wong, 2009). For salinity, if there is a small sensor drift, uncorrected salinities are accurate to ±0.1 psu, although this value can increase with increasing sensor drift. Delayed mode processing subjects all float profiles to detailed scrutiny, by comparison with historical data (Owens and Wong, 2009), providing corrected adjusted values while assigning each value with a quality flag.

Conservative Temperature, Absolute Salinity and potential density are determined from the in-situ temperature, practical salinity and pressure variables in the profile data, in accordance with TEOS-10 (IOC et al., 2010). Conservative Temperature is more representative of the "heat content" of seawater in comparison to potential temperature (McDougall and Barker, 2011). The profile data are linearly interpolated onto 41 dbar levels, ranging from 50 to 2000 dbar. The pressure levels used are shown in Table 1. Objective mapping is applied to the entire dataset spanning from December 2001 to March 2013, as well as to 3 sub-sets, where the data are split according to the following time periods: (1) 2002–2005, (2) 2006–2009 and (3) 2010–2013, which splits the dataset into roughly equal time spans. The profile distribution for the three time periods is shown in Fig. 2b–d while the respective profile densities (the number of profiles to a $3 \times 3^{\circ}$ grid cell) are shown in Fig. 4.

2.2 Sub-surface temperature maximum

In addition to the temperature and salinity maps of the 41 standardized pressure levels to which the profile data are interpolated, maps of temperature, salinity and pressure are also determined at the level of the sub-surface temperature maximum. Examples of typical Temperature–Pressure profiles from Argo float data within the Weddell Gyre are shown in Fig. 5. The sub-surface temperature maxima are clearly marked. There are two reasons for providing the sub-surface temperature maximum. Firstly, it represents the core of incoming Circumpolar Deep Water, which is the main source water feeding

ESSDD
8, 509–566, 2015

the Weddell Gyre. Secondly, it is used to define the northern boundary of the Weddell Gyre. The northern boundary is defined by the Weddell Front, which is controlled by the topography of the sub-surface ridges (e.g. the North Weddell ridge) but is not fixed in position due to strong interactions between the Antarctic Circumpolar Current to the north and the Weddell Gyre flow to the south. The Weddell Front can be located where the core of warm water from the Antarctic Circumpolar Current meets the relatively cold subsurface water of the Weddell Gyre (Fahrbach et al., 2011). Thus, the sub-surface temperature maximum is used to aptly define the latitude at which the meridional temperature gradients are the highest – which is the definition of the northern boundary of the Weddell Gyre in this study. The sub-surface temperature maximum is determined by taking the sum of the z scores of temperature and pressure. The z score assigns "scores" to data points based on their deviation from the mean. Using z scores instead of the standard deviations (from which the z scores are calculated) allows for the direct consideration of standard deviations from two different variables; here we seek the warmest temperature at the deepest depth, in order to ensure the sub-surface temperature maximum is selected rather than, for example, the summer surface water. The index of the sum of z scores with the smallest magnitude then represents the level of the sub-surface temperature minimum (i.e. the coldest water at the shallowest depth). The maximum sub-surface temperature can then be determined as the maximum temperature below the minimum. This method finds the deepest temperature maximum, thus taking into account seasonal surface warming.

2.3 Approach to objective mapping

Objective mapping was applied to Argo float data in order to produce spatially gridded fields of temperature and salinity for the upper ocean in the Weddell Gyre region. One requirement of objective mapping is to have knowledge of the mean field, $\langle x \rangle$, which, due to the irregular nature of the Argo array, presents a challenge and is the very motivation for objective mapping in the first place. Many studies involve the decomposition of measured fields into large and small scale components, where the subsequent large-

ESSDD
8, 509–566, 2015

scale field estimate is subtracted from the data. The resulting data residuals are used to determine the small scale component. The final mapped field estimate is the sum of the large- and small scale components. This way, the mean (first guess) field, $\langle x \rangle$, is a simple matter of taking the mean of the set of data, $\boldsymbol{x} = [x_1, \ldots, x_i]$, and the mean of the residuals of $\boldsymbol{x}$ for the small-scale component. Such studies stem from Roemmich (1983), and include Wong et al. (2003), Böhme and Send (2005) and Chang et al. (2009). Other studies provide an estimate of the mean (first guess) field using model output data, or climatology fields, such as in Hadfield et al. (2007). For the examples listed above, the mapping method is applied in regions where the hydrography is highly variable, and data are spatially and temporally abundant. Thus, the small-scale signal is essential in resolving small-scale features in both a spatial and temporal context.

By comparison, hydrography in the sub-surface Weddell Gyre is relatively invariant, and the volume of available data is considerably smaller, rendering such high-resolution mapped field variables unfeasible. There is always a compromise regarding the degree of detail achievable in a spatial context vs. a time context. In this study, the aim is to provide a broad outlook on the properties across the entire Weddell Gyre. Therefore a slightly different approach is chosen here. Firstly, rather than incorporate a temporal separation factor into the equation which assigns a weight to each data point, which would lead to a spatially and temporally regular gridded dataset, the data is split into sub-sets of time periods, so that the resulting maps represent spatially gridded time composites of the field variables for these time periods. This is due to the sparsity of the dataset. Secondly, the mapping process is implemented in a two-step procedure, allowing for a step-by-step improvement of the mean field estimate. In the first stage, the first guess field (in other words, the expected true value of the variable at the grid point location) is the zonal mean, calculated from all floats binned within the corresponding latitudinal boundaries, while the covariance is a function of large scale separation. The outcome is a large-scale estimate of the mapped field without consideration of smaller-scale features; this field estimate then becomes the first guess field in the second stage of mapping, where the covariance is a function of small-scale

ESSDD
8, 509–566, 2015

separation, which gives extra weight to close-by data in regions where the data are abundant. In regions of sparse data density, the objective estimate reverts back to the mean guess field and the corresponding mapping error is large. This 2-stage method reduces the possibility for errors by providing an improved estimate of the first guess field, which leads to a general reduction in the magnitude of the signal variance, $\langle s^2 \rangle$, by which the covariance matrices are scaled by. The error variance is calculated from the second stage of the mapping only.

2.4 Objective mapping

For each pressure surface, the corresponding temperature and salinity data are extracted from the vertically linearly interpolated float profiles (for further details refer to Sect. 2.1). Thus, only vertically interpolated data at the pressure surface to be mapped to are included in the mapping. The extracted data points are objectively mapped onto a regular $1^\circ \times (1^\circ/\cos(-65^\circ))$ grid. This results in grid cells of approximately 110 km × 110 km at 65° S; roughly the central axis of the gyre. For each grid point, N representative profiles (x) are selected for the mapping procedure (for details regarding the selection procedure, refer to Sect. 2.5). The objective estimate of the variable, X_{g1}, at the grid point g is given by Eq. (1a) for stage 1 and Eq. (1b) for stage 2. The zonal mean, $\overline{x}_z$, is the first guess field in stage 1 while the objective estimate from stage 1 becomes the first guess field used in stage 2. The term ω denotes the weighting matrix (Wong et al., 2003).

$$X_{g1} = \overline{x}_z + \omega \cdot \left(x - \overline{x}_z\right) \tag{1a}$$

$$X_{g2} = X_{g1} + \omega \cdot \left(x - X_{g1}\right) \tag{1b}$$

Each profile x is weighted by the horizontal distance D and the fractional distance F in potential vorticity: (1) between the grid point location g and the profile location i, and (2) between the neighbouring N profile locations, i and j. Thus, the profiles are not just weighted according to their distance to the grid point, but also to neighbouring

ESSDD
8, 509–566, 2015

profiles. As such, where three profiles may have the same distance to a grid point, the profile furthest apart from the neighbouring profiles will be assigned the largest weight (for example, refer to Fig. 6). The fractional distance F (Eq. 2) accounts for the cross-isobath separation between two locations. This reflects the influence of potential vorticity, and thus bathymetry (Fig. 7) and the Coriolis force (and therefore change in latitude); potential vorticity strongly influences the flow patterns of water masses, which is accounted for by (Böhme and Send, 2005):

$$F = \frac{|\mathrm{PV}(a) - \mathrm{PV}(b)|}{\sqrt{\mathrm{PV}^2(a) + \mathrm{PV}^2(b)}} \tag{2}$$

where a and b represent the locations of grid point g and profile i or the neighbouring N profile pairs, i and j. PV is the barotropic potential vorticity, $\mathrm{PV} = \frac{f}{H}$ where f is the Coriolis parameter and H is the full ocean depth, based on the general bathymetric chart of the oceans (GEBCO; IOC et al., 2003). The distances D and F are scaled by a horizontal length scale L ($L_{(\text{stage 1})} = 1000$ km and $L_{(\text{stage 2})} = 500$ km) and a cross-isobath scale ϕ ($F_{(\text{stage 1})} = 0.5$ and $F_{(\text{stage 2})} = 0.25$) respectively. See Sect. 2.5 for the reasoning behind the chosen values for L and F.

The decay scales determined by the distances D and F and their associated length scales are applied in the form of covariance functions in order to determine the weight matrix, ω (Eq. 3). The data-grid covariance ($\boldsymbol{C}_{\mathrm{dg}}$; Eq. 4) is a function of the distances between the grid point g and the profile location i while the data-data covariance ($\mathbf{C}_{\mathrm{dd}}$; Eq. 5) is a function of the distance between the N neighbouring profiles, i and j. Thus, for every grid point, while $\boldsymbol{C}_{\mathrm{dg}}$ is a $1 \times N$ vector, $\mathbf{C}_{\mathrm{dd}}$ is a $N \times N$ matrix. The covariance of the data is assumed to be Gaussian, following Böhme and Send (2005).

$$\omega = \boldsymbol{C}_{\mathrm{dg}} \cdot \left[\mathbf{C}_{\mathrm{dd}} + I \cdot \langle \eta^2 \rangle\right]^{-1} \tag{3}$$

$$\boldsymbol{C}_{\mathrm{dg}_i} = \langle s^2 \rangle \cdot \exp\left\{ - \left[\frac{D_{ig}^2}{L^2} + \frac{F_{ig}^2}{\phi^2} \right] \right\} \tag{4}$$

ESSDD
8, 509–566, 2015

$$\mathbf{C}_{\mathrm{dd}_{ij}} = \langle s^2 \rangle \cdot \exp\left\{ - \left[\frac{D_{ij}^2}{L^2} + \frac{F_{ij}^2}{\phi^2} \right] \right\} \quad (5)$$

$$\langle s^2 \rangle = \left(\frac{1}{N} \right) \sum_i \left(x_i - \overline{X} \right)^2 \quad (6)$$

$$\langle \eta^2 \rangle = \left(\frac{1}{2N} \right) \sum_i (x_i - x_n)^2 \quad (7)$$

The covariance functions are scaled by the signal variance, $\langle s^2 \rangle$ (Eq. 6), which measures the squared deviations of the data from the mean field. N is the number of profiles used to estimate the value at the grid point. The mean field $\overline{X}$, is the zonal mean in the first mapping stage while the objective estimate from stage 1 becomes the mean field in the second mapping stage. A random noise signal (i.e. the noise variance), $\langle \eta^2 \rangle$ (Eq. 7), is added to the diagonal of the data-data covariance function, where x_n is the variable of the profile with the smallest distance to the profile location i. This term accounts for the variations between nearby data.

In addition to providing an estimate of the field at locations where there are no data, objective mapping also provides an error variance of the objective estimate. This is taken from the second stage of the mapping:

$$\sigma_g^2 = \langle s^2 \rangle - \boldsymbol{C}_{\mathrm{dg}} \cdot \left[\mathbf{C}_{\mathrm{dd}} + I \cdot \langle \eta^2 \rangle \right]^{-1} \cdot \boldsymbol{C}_{\mathrm{dg}}^{\mathrm{T}} \quad (8)$$

where the superscript T signifies the transpose of the vector $\boldsymbol{C}_{\mathrm{dg}}$.

2.5 Choosing appropriate length scales (L, F) and selecting N surrounding data points to a grid point

In stage 1 of the mapping, the length scales are L = 1000 km and ϕ = 0.5 while in the second mapping stage, in order to give extra weight to nearby data points, L = 500 km

ESSDD
8, 509–566, 2015

and $\phi = 0.25$. Thus, a factor of 4 in the difference f/H is equivalent to a 500 km horizontal separation on the separation parameter; the decay scale used in the covariance functions (Hadfield et al., 2007). The performance of the objective mapping is sensitive to the length scales used in the correlation function. For a successful and accurate mapping of the field of variables, the applied length scales need to be larger than the minimum distance between data points. Otherwise, the mapped estimate will revert to the mean first guess field used in the mapping, and the resulting mapping error will be large. In order to establish suitable length scales for the mapping, the percentage of grid points with at least 40 data points within certain distances are calculated, in a similar manner to Hadfield et al. (2007). The results are shown in Fig. 8. The minimum distance where 100 % of the grid points have at least 40 data points for the entire time series is 1000 km. However, while the percentage remains high (about 99 %) for the time periods 2006–2009 and 2010–2013, the percentage decreases to about 95 % for the time period 2002–2005. At 500 km, about 95 % of the grid points have 40 or more data points for the entire time period; about 75, 93 and 90 % of the grid points have more than 40 data points within 500 km for the time periods 2002–2005, 2006–2009 and 2010–2013 respectively. This value rapidly decreases for distances less than 500 km. Therefore, 1000 km is used for the large length scale in the first mapping stage and 500 km is the small length scale L used in the second mapping stage. If a temporal separation factor were to be incorporated into the decay scale for the second stage of the mapping, the length scales would have to increase accordingly.

The number of data points (N) used in the calculation of the field estimate was set to 40. The decay scale of the data-grid covariance function ($D_{ig}^2/L^2 + F_{ig}^2/\phi^2$) was applied to the data with the large length scales of stage 1 ($L = 1000$ km and $F = 0.5$), and all corresponding data points where the decay scale was larger than 1 were filtered out (i.e. only data within the e-folding scale of the covariance function were selected; $D_{ig}^2/L^2 + F_{ig}^2/\phi^2 < 1$). Where more than 40 profiles were available within the decay scale limit, data were sub-selected by the shortest possible distance to the grid point (i.e. smallest decay scale values).

ESSDD
8, 509–566, 2015

At first, the mapping process was carried out for the sub-surface temperature maximum. The resulting field of conservative temperature was used to determine the northern boundary of the gyre: for each longitudinal bin, the latitude where the sub-surface temperature is more than 2 °C is masked. Following this, the latitude at which the meridional sub-surface temperature gradient is largest is defined as the position of the Weddell Front. All grid cells north of this latitude are masked in the following objective mapping processes. The mapping process is then carried out for 41 pressure surfaces, ranging from 50 to 2000 dbar.

2.6 Masking grid cells of high error variances

In addition to the mapped variables and associated mapping errors, error masks are also provided corresponding to the mapping errors of conservative temperature and absolute salinity. Where a grid cell mapping error passes the masking criteria, the grid cell is represented by the number 1; all other grid cells are represented by the fill value NaN. The method of defining the masking criteria is outlined as follows. Separate histograms of temperature and salinity mapping errors are created, where the grid cells are binned according to their error variances and a subsequent percentage of grid cells within each error variance bin are determined. A sample histogram (of conservative temperature at 800 dbar of the entire 11 year time composite) is shown in Fig. 9. The masking error criterion at 95 % is about 0.01 °C; all grid cells with an error variance that exceeds this value are masked and shown as slightly transparent in the maps presented in Sect. 3. The masking criterion is defined by the error value which is not exceeded by 95 % of the grid cells. Any grid cell where the corresponding mapping error is larger than the masking criterion is masked (by a 1 in the masking array). This is carried out separately for each vertical level of mapped variables. There are two masks – the "temperature mask" is based on the masking criterion from the temperature mapping error alone, whereas the salinity mask is based on the condition that if either temperature or salinity mapping errors exceed the corresponding masking criteria, the respective grid cell is masked (again with a 1 in the masking array). The

ESSDD
8, 509–566, 2015

masking criterion is determined from the error maps of the entire 11 year composite, as well as for each subset time composite period. The maps shown in Sect. 3 are masked according to the error maps of the entire 11 year composite, to show how the error variance increases with less available data (in particular, for example, in the time period from 2002 to 2005). The masks are applied in the form of a semi-transparent layer over the contour maps (see Sect. 3). For pressure at the level of the subsurface temperature maximum, the temperature mask is applied instead of a mask based on the pressure error map. This is because the subsurface temperature field is relatively stable, whereas the pressure is more dynamic. This is discussed further in Sect. 4.2.

3 Results

The following section describes the format of the dataset resulting from applying objective mapping to Argo float data and provides some examples of the subsequent mapped fields of data. The pressure and conservative temperature at the level of the sub-surface temperature maximum is presented for the entire 11 year time composite. Additionally, the mapped fields of conservative temperature and absolute salinity at 800 dbar are shown, along with the corresponding error variances, for the entire 11 year time composite and the three time period subsets (2002–2005, 2006–2009 and 2010–2013).

3.1 Data format: gridded fields of upper Weddell Gyre water properties

The time composite data sets of mapped field variables are provided as netCDF files; one file for each available time period. The filenames and corresponding variables provided in each netCDF file are listed in Tables 2 and 3 respectively. Mapped fields of conservative temperature (°C), absolute salinity ($g\,kg^{-1}$) and potential density ($kg\,m^{-3}$) are provided for 41 vertical pressure levels (listed in Table 1). Additionally, the three variables listed above, as well as pressure (dbar) at the level of the subsurface temper-

ESSDD
8, 509–566, 2015

ature maximum are provided (Sect. 2.2 details the method of identifying the subsurface temperature maximum). All mapped variables are provided alongside corresponding mapping errors and error masks (see Sect. 2.6 for a detailed explanation of the error masks). Information regarding the grid coordinates and vertical pressure levels are provided, where grid cell size is defined by 1° latitude ×1°/cos (−65°) longitude; latitude and longitude are described as −90 to 90° N and −180 to 180° E respectively. Further details found in the global attributes of the netCDF files are described throughout Sect. 2. The coordinates represent the centre of each grid cell. The missing value is defined by NaN. Additional information regarding the units of variables and the structure of the corresponding data array (i.e. latitude × longitude × vertical pressure level) are detailed in the attributes of each variable, and are also detailed throughout this paper.

3.2 Sub-surface conservative temperature maximum

A typical feature in the hydrography of polar regions is the presence of a sub-surface temperature maximum, as displayed in Fig. 5, which results from influx of warmer waters from lower latitudes. The maps in Fig. 10 present conservative temperature, Θ, at the level of the sub-surface temperature maximum, for the entire time series from 2002 to March 2013. Figure 10a displays the original float profiles while Fig. 10b shows the mapped field of $\Theta_{(\Theta max)}$. The associated mapping error is provided in Fig. 10c. Note the translucent contours within Fig. 10b mark the regions of high error marked by the dark red contours in the mapping error of Fig. 10c (for detailed explanation, refer to Sect. 2.6). This occurs for all contour maps presented in this paper. The boundary of the gyre to the north is clear as a sharp transition between warmer temperatures above 2 °C to the north and cooler temperatures of the gyre below 1 °C to the south. This boundary reflects the bathymetry of the region, including the northern extension of the gyre at the South Sandwich Trench (just east of 30° W, 53 to 60° S). The incoming source water of the Circumpolar Deep Water is also shown as a core of warm water entering the gyre in the east, in the southern limb of the gyre (at about 65° S, 30° E). This warm water cools from about 1.2 to 0.6 °C as it circulates westwards through the

ESSDD
8, 509–566, 2015

southern limb of the gyre. A double gyre structure is also suggested, where the secondary gyre occurs in the north-east sector, splitting from the main gyre at about 5° W. The associated mapping error is relatively small, with the largest errors occurring at the gyre boundary, particularly in regions of complex bathymetry. The error is small within the gyre, even in regions of especially sparse data density (with the exception of 45–55° W, 64–72° S, where no profile floats are located within the region). This is because the temperature field is relatively stable, which results in a small signal variance field. The field of pressure at the sub-surface temperature maximum, $Pr_{(\Theta max)}$, Fig. 11, is less stable in comparison to $\Theta_{(\Theta max)}$, which is why the error (Fig. 11c) is larger, again at the gyre periphery as well as along the Antarctic coast. There is also a considerable deepening of the sub-surface temperature maximum at about 65° S, just east of the Prime Meridian, from about 200 m in the surrounding region to roughly 400 m, which occurs directly over Maud Rise (note the mapping error is relatively small in this region). The sub-surface temperature maximum is shallowest within the gyre centre, and deepest towards the gyre peripheries, demonstrating the domed structure associated with the cyclonicity of the gyre.

The mean meridional sub-surface temperature, $\Theta_{(\Theta max)}$ along the Prime Meridian (as extracted from the corresponding objectively mapped gridded data set) is given in Fig. 12a along with the resultant meridional temperature gradient in Fig. 12b. The large dots show the latitude at which the gradient is largest, which occurs at 56° S (note: the gradient is negative due to the south–north direction). This is the latitude used to define the northern boundary at the Prime Meridian, which corresponds with the northern boundary used in the long-term analysis of properties at the Prime Meridian in Fahrbach et al. (2011). All grid points north of this latitude are masked from the mapping process for the subsequent isobaric mapped surfaces.

3.3 An example: Θ and S_A at 800 dbar

Figure 13a–c shows the original profile data, the mapped field and the associated mapping errors respectively, of conservative temperature at 800 dbar, for the entire time

ESSDD
8, 509–566, 2015

period from 2002 to 2013. Figure 14 shows the same but for absolute salinity, S_A. The temperature field shows the structure of the gyre, where relatively warm water from the north enters the gyre in the southern limb (south of 60° S) at about 30° E and gradually cools as it circulates in a clockwise direction throughout the gyre. There is a gradual transition from relatively warm water in the south east sector of the gyre, to cooler water in the western southern limb of the gyre, to even cooler water in the northern limb of the gyre. The coolest water at 800 dbar occurs in the east within the northern limb of the gyre. The cyclonic-gyre signal is less clear in the absolute salinity field (Fig. 14b). Regardless, there is a gradual freshening from the southern limb to the northern limb of the gyre, consistent with the cooling spatial trend. Again, the associated mapping errors are small, in particular in the centre of the gyre, and larger in regions of complex bathymetry at the gyre boundaries.

Figure 15a–c shows the mapped conservative temperature fields at 800 dbar for data sub-sampled to the time periods 2002–2005, 2006–2009 and 2010–2013 respectively, while Fig. 15d–f shows the corresponding mapping errors. The temperature fields represent the gyre structure with the water cooling as it transitions from the southern limb to the northern limb in a clockwise direction. While the northern boundary appears to be relatively stable, with minimal change across the three time periods, the region where warm water enters from the east varies with each time period. The warmest signal that extends furthest into the gyre (about 1 °C) occurs in 2006–2009 (Fig. 15b). However, the error associated with this region (Fig. 15e; about 10–30° E, 62–68° S) is relatively large, due to a considerable data gap that can be seen in Fig. 2c. There is also a large data gap and associated mapping error for 2010–2013 (Fig. 2d and Fig. 15f respectively). Figure 16 shows the same as Fig. 15 but for absolute salinity. Again the freshest signal occurs in the northern limb. The southern limb appears to be saltier in the first time period (2002–2005), particularly in comparison to the second time period (2006–2009). The errors in Fig. 16d–f are smaller in comparison to the temperature fields due to a smaller signal variance.

ESSDD
8, 509–566, 2015

4 Discussion

The following Section assesses the performance of the objective mapping method (outlined in Sect. 2) in providing gridded fields of water column properties of the upper 2000 m of the entire Weddell Gyre. Certain decisions regarding the mapping method are discussed and potential implications are highlighted. Additionally, the mapping errors are carefully considered in terms of the likely causes of large error variances in certain regions. Lastly, in place of a regular grid, the profiles were objectively mapped to the locations of the profiles themselves in order to directly gauge the performance of the mapping process, by assessing the difference between the original data and the mapped product.

4.1 Objective mapping performance

Argo float data were objectively interpolated in order to provide gridded fields of water column properties of the upper 2000 m of the Weddell Gyre. By comparing the scatter-grams of the original data (e.g. Fig. 13a) to the corresponding mapped products (e.g. Fig. 13b), it is clear that the objective mapping method performs generally well in producing regularly gridded fields of (i) temperature at the sub-surface temperature maximum (Fig. 10b), and (ii) of temperature and salinity at 800 dbar (e.g. Fig. 13b and Fig. 14b respectively). In addition, the associated mapping errors are relatively small throughout (e.g. Fig. 13c); less than 0.01 °C across the majority of the Weddell Gyre in Fig. 15d–f. The discernable general hydrographic features of Figs. 10–16 are also to be expected; the cyclonicity of the gyre is demonstrated by the relatively cool gyre interior (e.g. Fig. 13b). Furthermore, shoaling of the sub-surface temperature maximum occurs at the centre (Fig. 11b), exhibiting the dome-like structure of the gyre as discussed by Orsi et al. (1993) and Fahrbach et al. (2011). By assessing the spatial variability of temperature across the three time periods in Fig. 15a–c, it is clear that the temperature in the eastern sector of the gyre's southern limb is more variable than both the cooler gyre interior and the western sector of the southern limb. This is due to the

ESSDD
8, 509–566, 2015

variability of the incoming source water, Circumpolar Deep Water, which is influenced by the variability of the Antarctic Circumpolar Current and possibly wind forcing of the Weddell Gyre (Fahrbach et al., 2011; Cisewski et al., 2011). Additionally, the influence of Maud Rise leads to increased spatial variability in the region; such as a deepening of the sub-surface temperature maximum in Fig. 11b and a regional cooling at 800 dbar across all three time periods in Fig. 15 (although the cooling is so slight during the first time period (2002–2005) that the contour levels in Fig. 15a fail to resolve the localised cooling). The cooling and freshening over Maud Rise at 800 dbar (Figs. 13b and 14b respectively), along with the deepening of a cooler temperature maximum, represents trapped water in a Taylor Column and shows agreement with Bersch et al. (1992), Muench et al. (2001) and Leach et al. (2011). The factors discussed above could explain the variability of Warm Deep Water along the Prime Meridian as observed and discussed by Fahrbach et al. (2011). However, considerable data gaps within the eastern sector of the southern limb, especially for the latter two time periods (e.g. Fig. 2c and d), render it challenging to draw concrete observations for this region. The importance of establishing efforts to monitor this region is becoming increasingly recognized, due to the potential contribution of incoming deep water masses from further east on the export of Antarctic Bottom Water to the lower limb of the global oceanic overturning circulation (Meredith et al., 2000, 2014; Jullion et al., 2014).

There appears to be two main influences determining the magnitude of the mapping error variances throughout the Weddell Gyre. The mapping error is typically large in regions of sparse data coverage (e.g. in the south-west corner of the Weddell Sea in Fig. 10c), which is especially prominent in the first time period, as shown by the large masked area in Fig. 15a (the masked areas are semi-transparent and mark regions where the mapping error is larger than 0.007 °C; see Sect. 2.6 for an explanation of the error masks). However, there are also regions of dense data coverage where the mapping errors are also relatively large (e.g. at about 60° S, west of 45° W, in Fig. 13c). In particular, the north-west corner of the gyre has relatively high mapping errors throughout all maps. This is due to the dynamic nature of the region. The

ESSDD
8, 509–566, 2015

bathymetry is complex due to the presence of submerged ridges and trenches. It is also at the very periphery of the gyre where complex interaction with the Antarctic Circumpolar Current takes place (e.g. Klatt et al., 2005; Fahrbach et al., 2004, 2011; Cisewski et al., 2011). Thus, the objective mapping is poorly representative of these highly variable, complex regions. One way to improve the objective estimate of these regions is to incorporate more suitable correlation length scales as well as a temporal separation factor into the decay scale in Eqs. (4) and (5), such as in Böhme and Send (2005). The correlation length scales would need to match the scale of the true field in order to adequately map these regions. Since these regions typically only occur at the very periphery of the gyre, and due to data sparsity throughout the relatively invariant inner gyre, the correlation length scales are chosen to represent the large scale field of the entire gyre, as opposed to a small-scale, temporally scaled field of a smaller area of the gyre (since the mapping would be restricted to regions where there are enough data to perform the interpolation). Additionally, the incorporation of a temporal separation factor would require an increase in the correlation length scales in Eqs. (4) and (5), in order to provide an adequate number of data points which exist within the e-folding scale ($D_{ig}^2/L^2 + F_{ig}^2/\phi^2 < 1$, see Sect. 2.5). 1000 km, the horizontal length scale for the first mapping stage, incorporates about 9° in the Meridional direction. Since the gyre generally spans about 10–15° in the Meridional direction, a larger length scale would draw on data from outside the gyre, thus reducing the quality of the mapping. In order to reduce the correlation length scales as is sensibly possible in obtaining a gyre-scale view of the Weddell Gyre hydrography, while at the same time assessing variability in a temporal context, a compromise is reached by way of creating temporal composites of three time periods. Regardless, the mapping errors are relatively large in regions of sparse data coverage within the gyre across all three time periods. This is most prevalent in the first time period, 2002–2005, where the mapping error (Fig. 15d) across the west and north-west sector of the gyre is masked out in Fig. 15a due to failure of the masking criterion (i.e. masked by transparency; see Sect. 2.6); the largest mapping error of this region is 0.65 °C. This can be directly associated with little data

ESSDD
8, 509–566, 2015

availability in Fig. 2b. There are also areas of limited data coverage in the time period 2006–2009 (Fig. 2c) and in the time period 2010–March 2013 (Fig. 2d), both at about 20° E, south of 60° S, which lead to maximum mapping errors of 0.035 and 0.06 °C in Fig. 15e and f respectively. Thus, while steps were made to optimise the quality of the objective mapping based on the limited data available (e.g. Fig. 8), it is important to assess the corresponding mapping errors when interpreting the gridded fields of data, particularly the sub-sets of the three time periods, especially due to regions of limited data availability. Furthermore, across all maps, the region of most prevalent mapping errors occurs at the northern boundary of the gyre. Where the meridional gradients of the sub-surface temperature maximum are largest defines the northern boundary of the gyre, which coincides with these regions of relatively large mapping errors. Therefore it is important to acknowledge that the definition used for the northern boundary in this study is sensitive to the associated mapping error variances in Fig. 10c.

Mapping errors vary according to the corresponding pressure level. Figure 17a and b shows the vertical variation of the error mask limits (based on the 95 % error value, i.e. 95 % of grid points have a smaller error than the 95 % limit; for an explanation of the error masks, see Sect. 2.6) for conservative temperature and absolute salinity respectively. While the error limits are relatively invariant below 400 dbar, there is a considerable change in shallower waters. With the exception of the time period 2002–2005, where the error limit monotonically increases in magnitude from about 200 to 50 dbar for temperature, and from about 400 to less than 200 dbar for salinity, the remaining time periods show a peak in error limit at about 120–180 dbar and a relatively small minimum at about 70 dbar for temperature. Regarding salinity, the error limit more or less increases with decreasing pressure, although a peak maximum (minimum) error occurs at about 100 (70) dbar for the time period 2010–2013, and 180 (100) dbar for the entire time period. This coincides with the region of Winter Water, where the peak in the error limit for temperature occurs at the approximate depth of the lower boundary (e.g. see Fig. 3 in Behrendt et al., 2011). Thus seasonal signals may have led to

ESSDD
8, 509–566, 2015

the increase of the mapping errors in the shallower mapped surfaces, which should be taken into account when interpreting the mapped surfaces above 200 dbar.

In addition to regions of dynamic hydrography and regions of low data density, a further potential factor influencing the mapped data output is linked to the selection process of N representative profiles for each grid point objective estimate. Many studies incorporate a decision process whereby one third of the profiles are randomly selected from within the e-folding scale of the covariance function in Eqs. (4) and (5); (i.e. $D_{ig}^2/L^2 + F_{ig}^2/\phi^2 < 1$), one third are selected with the smallest distance within the large correlation length scales, and the remaining third of profiles are selected with the shortest spatial and temporal separation distances (e.g. Rabe et al., 2011; Böhme and Send, 2005). This was done in order to remove potential bias by selecting nearby profiles, such as, for example, those from along repeat hydrographic sections, which are closely spaced in both distance and time. In this study, only data within the e-folding scale of stage 1 are selected, in accordance with the studies above. Where there are more than $N(N = 40)$ profiles available, the N profiles with the smallest spatial separations are simply selected. This is justified because the only data utilized comes from Argo floats, which are independent of repeat-ocean transects. Furthermore, it is a necessary compensation due to limited data availability (and thus the necessity of large correlation scales).

Another source of error which must be taken into consideration concerns the winter profiles that have become available since 2007, when a "sea-ice sensing" algorithm allowed for the survival of floats in regions of sea-ice cover (Klatt et al., 2007). While these floats provide profiles that would otherwise be unavailable due to sea-ice, an important assumption has been made regarding the corresponding "under-ice" profile positions. The position of these profiles is estimated by linear interpolation between the last known position of the float before it enters the sea-ice zone, and the first known position of the float upon exiting the sea-ice zone. Thus, the positions of these floats are clearly incorrect. Examples of such profiles can be seen in Fig. 2d: there are profiles that are distributed along straight lines, particularly in the south west sector of the gyre.

ESSDD
8, 509–566, 2015

It is therefore a priority to improve the position estimates of such floats. However, such profiles within the gyre interior do not appear to increase the mapping error of the mapped surfaces, reflective of the stable, relatively invariant gyre interior. The regions where these profiles may increase the mapping error are along the Antarctic coastline where complex bathymetry, lack of available profiles, and interaction between the flow of the incoming Circumpolar Deep Water and the cold, westward Antarctic coastal current also play a role in increasing the mapping error.

4.2 Mapping the sub-surface temperature maximum: two approaches compared

When mapping to the level of the sub-surface temperature maximum, there are two approaches one can make. One approach is to extract the corresponding pressure, temperature and salinity values at the sub-surface temperature maximum for every float profile in the dataset and map each variable independently. This is the approach outlined in Sect. 2.2. Another approach is to extract the pressure of the sub-surface temperature maximum for each float profile and apply objective mapping to the pressure variable alone in order to determine a regular gridded dataset of pressure at the level of the sub-surface temperature maximum. For each grid point, one then selects the N closest profiles, from which the temperature and salinity values are extracted at the pressure level provided by the mapped field previously determined. Thus, the resulting mapped fields of temperature and salinity are dependent on the mapped pressure of the sub-surface temperature maximum rather than the individual profiles themselves. Both approaches were investigated and compared for the entire time period from 2002 to March 2013. The resulting mapped field of temperature and the corresponding mapping error are shown in Fig. 10b and c respectively for the first approach, and in Fig. 18a and b respectively for the second approach. The mapped temperature fields for the two approaches are similar. The differences between the two temperature maps is less than 0.2 °C throughout the Weddell Gyre, with the exception of regions at the gyre periphery where the differences can be as high as 0.4 °C (Fig. 19). The first

ESSDD
8, 509–566, 2015

approach typically yields warmer values than the second approach throughout most of the region (hence the map in Fig. 19 is largely negative (blue), as it shows temperature from approach 2 w.r.t temperature from approach 1). The second approach leads to slightly larger mapping errors, in particular along the Antarctic coastline. Thus, the first approach, where the temperature, salinity and pressure of the sub-surface temperature maximum are independently mapped, is the approach followed in this study.

Pressure at the level of the sub-surface temperature maximum has the largest corresponding mapping errors of all mapped surfaces, despite the relatively small errors in the mapping of conservative temperature at the sub-surface temperature maximum. This is because it is subjective to allocate a specific point at which the temperature has reached its maximum in many of the profiles. Although a statistical method is employed here (see Sect. 2.2), the processes that influence the position of the temperature maximum are too complex for the method to be extremely accurate, and the number of profiles are too numerous to identify each peak manually. Some profiles do not have a pronounced sub-surface temperature maximum. The peak temperature then occurs with a small vertical gradient, so a small change in temperature could shift the peak temperature by 100s of meters. Thus, while the mapping of the sub-surface temperature maximum is relatively successful, caution needs to be made when considering the pressure at the level of the sub-surface temperature maximum. It is primarily for this reason that the second approach described above was not used in the mapping process.

4.3 Objective Mapping to float profile locations

In addition to objectively mapping Argo float data to a grid to create a spatially regular field of data variables, the profile data were also objectively mapped to the locations of the profiles themselves, in order to assess the performance of the objective mapping procedure. It is important to note that the resulting maps should not precisely match the profile data, due to the assumption of noise in the dataset ($\langle \eta^2 \rangle$; Eq. 7). While the objective mapping was carried out at the level of the sub-surface temperature maxi-

ESSDD
8, 509–566, 2015

mum as well as at 800 dbar, only the latter is presented here. Figure 20a shows the original profile data of conservative temperature at 800 dbar for the entire time period 2002–2013. Figure 20b shows the objectively mapped field estimate, mapped to the profile locations, while Fig. 20c shows the difference, where the mapped profile data has been subtracted from the original data (i.e. Fig. 20a minus Fig. 20b). The mapping process performs well particularly within the gyre centre, where the differences for the profile locations within the gyre are less than ±0.2 °C. The differences are larger north of the gyre (mostly north of 60° S), especially in the bathymetrically complex region west of 15° W (i.e. approaching Drakes Passage). This is outside of the Weddell Gyre region, yet may influence the accuracy of the northern boundary of the gyre. Taking into account all data points shown in Fig. 20c, 87 % of the data points have differences between the original data and the mapped data that are within ±0.2 °C (Fig. 21a). Furthermore, by considering only profiles within the gyre itself (using the northern boundary definition described in Sect. 2.2), 89 % of the mapped data points differ from the original data points by ±0.2 °C (Fig. 21b). Regarding sub-surface temperature maximum (Fig. 22), 82 % (84 %) of the mapped data points differ to the original data by utmost ±0.2 °C for the entire data set (for only those profiles within the Weddell Gyre). Lastly, for pressure at the sub-surface temperature maximum, 77 % of the mapped data points differ from the original data points by ±100 m (Fig. 23a); this value increases to 84 % when considering just those profiles within the Weddell Gyre (Fig. 23b).

5 Concluding remarks

The objective of this paper was to provide a spatially gridded dataset of the upper 2000 m of the water column properties of the entire Weddell Gyre region. Objective Mapping was applied in a two-step process to Argo float profile data spanning December 2001 to March 2013 and to sub-sets of the float data for the 2002–2005, 2006–2009 and 2010–March 2013 periods. Maps of pressure, conservative temperature and absolute salinity are provided at the level of the sub-surface temperature maximum, and

ESSDD
8, 509–566, 2015

maps of conservative temperature and absolute salinity are provided at 41 standardized pressure levels ranging from 50 to 2000 dbar. The corresponding mapping errors are also provided. The resulting mapped fields provide a more complete as well as more detailed view of the pertinent features of the Weddell Gyre, such as the doming of the gyre centre owing to its cyclonic rotation and the associated relatively cool gyre interior, than existed before. The relatively warm incoming source water at the eastern sector of the southern limb is also visible, along with the variability of water properties owing to bathymetric features such as Maud Rise. The mapping errors corresponding to the mapped field variables are relatively small, with the exception of regions where the bathymetry is complex, or where data coverage is limited. The mapping errors vary with pressure, where the overall largest mapping errors coincide with the region of Winter Water, particularly within the vicinity of its lower boundary (about 120–180 dbar). In order to gauge the performance of the mapping procedure, objective mapping was also applied to the location of the float profiles themselves. The objective mapping successfully represents the Weddell Gyre in its entirety, whereby 89 % of mapped profiles within the Weddell Gyre differ from the original profile values (for temperature at 800 dbar) by less than 0.2 °C. Caution should be taken in consideration of the increased error variances at the gyre periphery, in regions of limited data coverage, and due to the fact that all mapped fields are spatially gridded temporal composites. The work presented here provides the prerequisite technical component of investigations into the variability of Weddell Gyre water mass properties, providing further insight to the role of the Weddell Gyre in a changing climate.

Acknowledgements. These data were collected and made freely available by the International Argo Program and the national programs that contribute to it (http://www.argo.ucsd.edu, http://argo.jcommops.org). The Argo Program is part of the Global Ocean Observing System. The GEBCO Digital Atlas is published by the British Oceanographic Data Centre on behalf of IOC and IHO, 2003. This work is dedicated in memory of Eberhard Fahrbach (who passed away on the 21 April 2013), a great Polar Oceanographer who championed the observation of the Polar Oceans and was an inspiration to us all.

ESSDD
8, 509–566, 2015

References

Abraham, J. P., Baringer, M., Bindoff, N. L., Boyer, T., Cheng, L. J., Church, J. A., Conroy, J. L., Domingues, C. M., Fasullo, J. T., Gilson, J., Goni, G., Good, S. A., Gorman, J. M., Gouretski, V., Ishii, M., Johnson, G. C., Kizu, S., Lyman, J. M., Macdonald, A. M., Minkowycz, W. J., Moffitt, S. E., Palmer, M. D., Piola, A. R., Reseghetti, F., Schuckmann, K., Trenberth, K. E., Velicogna, I., and Willis, J. K.: A review of global ocean temperature observations: implications for ocean heat content estimates and climate change, Rev. Geophys., 51, 450–483, doi:10.1002/rog.20022, 2013.

Azaneu, M., Kerr, R., Mata, M. M., and Garcia, C. A. E.: Trends in the deep southern ocean (1958–2010): implications for antarctic bottom water properties and volume export, J. Geophys. Res.-Oceans, 118, 4213–4227, doi:10.1002/jgrc.20303, 2013.

Behrendt, A., Fahrbach, E., Hoppema, M., Rohardt, G., Boebel, O., Klatt, O., Wisotzki, A., and Witte, H.: Variations of winter water properties and sea ice along the greenwich meridian on decadal time scales, Deep-Sea Res. Pt. II, 58, 2524–2532, doi:10.1016/j.dsr2.2011.07.001, 2011.

Bersch, M., Becker, G. A., Frey, H., and Koltermann, K. P.: Topographic effects of the Maud Rise on the stratification and circulation of the Weddell Gyre, Deep-Sea Res., 39, 303–331, 1992.

Böhme, L. and Send, U.: Objective analyses of hydrographic data for referencing profiling float salinities in highly variable environments, Deep-Sea Res. Pt. II, 52, 651–664, doi:10.1016/j.dsr2.2004.12.014, 2005.

Boning, C. W., Dispert, A., Visbeck, M., Rintoul, S. R., and Schwarzkopf, F. U.: The response of the antarctic circumpolar current to recent climate change, Nat. Geosci., 1, 864–869, 2008.

Bretherton, F. P., Davis, R. E., and Fandry, C. B.: A technique for objective analysis and design of oceanographic experiments applied to mode-73, Deep-Sea Res. Oceanographic Abstracts, 23, 559–582, doi:10.1016/0011-7471(76)90001-2, 1976.

Chang, Y.-S., Rosati, A. J., Zhang, S., and Harrison, M. J.: Objective analysis of monthly temperature and salinity for the world ocean in the 21st century: comparison with world ocean atlas and application to assimilation validation, J. Geophys. Res.-Oceans, 114, C02014, doi:10.1029/2008jc004970, 2009.

ESSDD
8, 509–566, 2015

Cisewski, B., Strass, V., and Leach, H.: Circulation and transport of water masses in the Lazarev Sea, Antarctica, during summer and winter 2006, Deep-Sea Res. Pt. I, 58, 186–199, doi:10.1016/j.dsr.2010.12.001, 2011.

Couldrey, M. P., Jullion, L., Naveira Garabato, A. C., Rye, C., Herráiz-Borreguero, L., Brown, P. J., Meredith, M. P., and Speer, K. L.: Remotely induced warming of antarctic bottom water in the eastern weddell gyre, Geophys. Res. Lett., 40, 2755–2760, doi:10.1002/grl.50526, 2013.

Fahrbach, E. and de Baar, H.: The expedition of the research vessel "polarstern" to the antarctic in 2008 (ant-xxiv/3), in: Polar- und Meeresforschung 606, AWI, Bremerhaven, 228, 2010.

Fahrbach, E., Rohardt, G., Schröder, M., and Strass, V.: Transport and structure of the Weddell Gyre, Ann. Geophys., 12, 840–855, doi:10.1007/s00585-994-0840-7, 1994.

Fahrbach, E., Rohardt, G., Scheele, N., Schröder, M., Strass, V., and Wisotzki, A.: Formation and discharge of deep and bottom water in the northwestern Weddell Sea, J. Mar. Res., 53, 515–538, 1995.

Fahrbach, E., Hoppema, M., Rohardt, G., Schröder, M., and Wisotzki, A.: Decadal-scale variations of water mass properties in the deep weddell sea, Ocean Dynam., 54, 77–91, doi:10.1007/s10236-003-0082-3, 2004.

Fahrbach, E., Rohardt, G., and Sieger, R.: 25 years of polarstern hydrography (1982–2007), WDC-MARE Reports 5, Alfred-Wegener-Institut, Bremerhaven, 94 pp., 2007.

Fahrbach, E., Hoppema, M., Rohardt, G., Boebel, O., Klatt, O., and Wisotzki, A.: Warming of deep and abyssal water masses along the greenwich meridian on decadal time scales: the weddell gyre as a heat buffer, Deep-Sea Res. Pt. II, 58, 2509–2523, doi:10.1016/j.dsr2.2011.06.007, 2011.

Foster, T. D., Foldvik, A., and Middleton, J. H.: Mixing and bottom water formation in the shelf break region of the southern weddell sea, Deep-Sea Res., 34, 1771–1794, doi:10.1016/0198-0149(87)90053-7, 1987.

Gandin, L. S.: Objective Analysis of Meteorological Fields, Israel Program for Scientific Translations, Jerusalem, 1965.

Gille, S. T.: Decadal-scale temperature trends in the Southern Hemisphere ocean, J. Climate, 21, 4749–4765, doi:10.1175/2008jcli2131.1, 2008.

Hadfield, R. E., Wells, N. C., Josey, S. A., and Hirschi, J. J. M.: On the accuracy of north atlantic temperature and heat storage fields from argo, J. Geophys. Res.-Oceans, 112, C01009, doi:10.1029/2006jc003825, 2007.

ESSDD
8, 509–566, 2015

IOC, IHO, and BODC: Centenary edition of the gebco digital atlas, in: Published on CD-ROM on behalf of the Intergovernmental Oceanographic Commission and the International Hydrographic Organization as part of the General Bathymetric Chart of the Oceans, British Oceanographic Data Centre, Liverpool, 2003.

IOC, SCOR, and IAPSO: The International Thermodynamic Equation of Seawater – 2010: Calculation and Use of Thermodynamic Properties, Intergovernmental Oceanographic Commision, 196, 2010.

Johnson, G. C.: Quantifying antarctic bottom water and north atlantic deep water volumes, J. Geophys. Res.-Oceans, 113, C05027, doi:10.1029/2007jc004477, 2008.

Jullion, L., Garabato, A. C. N., Bacon, S., Meredith, M. P., Brown, P. J., Torres-Valdés, S., Speer, K. G., Holland, P. R., Dong, J., Bakker, D., Hoppema, M., Loose, B., Venables, H. J., Jenkins, W. J., Messias, M.-J., and Fahrbach, E.: The contribution of the weddell gyre to the lower limb of the global overturning circulation, J. Geophys. Res.-Oceans, 119, 3357–3377, doi:10.1002/2013jc009725, 2014.

Klatt, O., Fahrbach, E., Hoppema, M., and Rohardt, G.: The transport of the weddell gyre across the prime meridian, Deep-Sea Res. Pt. II, 52, 513–528, doi:10.1016/j.dsr2.2004.12.015, 2005.

Klatt, O., Boebel, O., and Fahrbach, E.: A profiling float's sense of ice, J. Atmos. Ocean. Tech., 24, 1301–1308, doi:10.1175/jtech2026.1, 2007.

Leach, H., Strass, V., and Cisewski, B.: Modification by lateral mixing of the warm deep water entering the Weddell Sea in the Maud Rise Region, Ocean Dynam., 61, 51–68, doi:10.1007/s10236-010-0342-y, 2011.

Levitus, S., Antonov, J. I., Boyer, T. P., Baranova, O. K., Garcia, H. E., Locarnini, R. A., Mishonov, A. V., Reagan, J. R., Seidov, D., Yarosh, E. S., and Zweng, M. M.: World ocean heat content and thermosteric sea level change (0–2000 m), 1955–2010, Geophys. Res. Lett., 39, L10603, doi:10.1029/2012gl051106, 2012.

Lyman, J. M. and Johnson, G. C.: Estimating annual global upper-ocean heat content anomalies despite irregular in situ ocean sampling, J. Climate, 21, 5629–5641, doi:10.1175/2008jcli2259.1, 2008.

Lyman, J. M., Good, S. A., Gouretski, V. V., Ishii, M., Johnson, G. C., Palmer, M. D., Smith, D. M., and Willis, J. K.: Robust warming of the global upper ocean, Nature, 465, 334–337, 2010.

McDougall, T. J. and Barker, P. M.: Getting Started with TEOS-10 and the Gibbs Seawater (GSW) Oceanographic Toolbox, SCOR/IAPSO WG127, 28 pp., 2011.

ESSDD
8, 509–566, 2015

McIntosh, P. C.: Oceanographic data interpolation: objective analysis and splines, J. Geophys. Res.-Oceans, 95, 13529–13541, doi:10.1029/JC095iC08p13529, 1990.
Meredith, M. P., Locarnini, R. A., Van Scoy, K. A., Watson, A. J., Heywood, K. J., and King, B. A.: On the sources of weddell gyre antarctic bottom water, J. Geophys. Res.-Oceans, 105, 1093–1104, doi:10.1029/1999jc900263, 2000.
Meredith, M. P., Jullion, L., Brown, P. J., Garabato, A. C. N., and Couldrey, M. P.: Dense waters of the Weddell and Scotia seas: recent changes in properties and circulation, Philos. T. R. Soc. A, 372, 20130041, doi:10.1098/Rsta.2013.0041, 2014.
Muench, R. D., Morison, J. H., Padman, L., Martinson, D., Schlosser, P., Huber, B., and Hohmann, R.: Maud Rise revisited, J. Geophys. Res., 106, 2423–2440, 2001.
Orsi, A. H., Nowlin Jr., W. D., and Whitworth III, T.: On the circulation and stratification of the weddell gyre, Deep-Sea Res. Pt. I, 40, 169–203, doi:10.1016/0967-0637(93)90060-G, 1993.
Orsi, A. H., Johnson, G. C., and Bullister, J. L.: Circulation, mixing, and production of antarctic bottom water, Prog. Oceanogr., 43, 55–109, doi:10.1016/S0079-6611(99)00004-X, 1999.
Owens, W. B. and Wong, A. P. S.: An improved calibration method for the drift of the conductivity sensor on autonomous ctd profiling floats by θ–s climatology, Deep-Sea Res. Pt. I, 56, 450–457, doi:10.1016/j.dsr.2008.09.008, 2009.
Purkey, S. G. and Johnson, G. C.: Antarctic bottom water warming and freshening: contributions to sea level rise, ocean freshwater budgets, and global heat gain, J. Climate, 26, 6105–6122, doi:10.1175/jcli-d-12-00834.1, 2013.
Rabe, B., Karcher, M., Schauer, U., Toole, J. M., Krishfield, R. A., Pisarev, S., Kauker, F., Gerdes, R., and Kikuchi, T.: An assessment of arctic ocean freshwater content changes from the 1990s to the 2006–2008 period, Deep-Sea Res. Pt. I, 58, 173–185, doi:10.1016/j.dsr.2010.12.002, 2011.
Robertson, R., Visbeck, M., Gordon, A. L., and Fahrbach, E.: Long-term temperature trends in the deep waters of the weddell sea, Deep-Sea Res. Pt. II, 49, 4791–4806, doi:10.1016/S0967-0645(02)00159-5, 2002.
Roemmich, D.: Optimal estimation of hydrographic station data and derived fields, J. Phys. Oceanogr., 13, 1544–1549, doi:10.1175/1520-0485(1983)013<1544:oeohsd>2.0.co;2, 1983.
Roemmich, D. and Gilson, J.: The 2004–2008 mean and annual cycle of temperature, salinity, and steric height in the global ocean from the argo program, Prog. Oceanogr., 82, 81–100, doi:10.1016/j.pocean.2009.03.004, 2009.

ESSDD
8, 509–566, 2015

von Schuckmann, K. and Le Traon, P.-Y.: How well can we derive global ocean indicators from Argo data?, Ocean Sci., 7, 783–791, doi:10.5194/os-7-783-2011, 2011.

Wong, A. P. S., Johnson, G. C., and Owens, W. B.: Delayed-mode calibration of autonomous ctd profiling float salinity data by θ–s climatology, J. Atmos. Ocean. Tech., 20, 308–318, doi:10.1175/1520-0426(2003)020<0308:dmcoac>2.0.co;2, 2003.

ESSDD

8, 509–566, 2015

Table 1. Standardized pressure levels (dbar) to which all profiles are linearly interpolated. The vertical levels within the corresponding mapped variable matrices are highlighted in bold (i.e. the shape of the matrices are as follows: latitude × longitude × pressure).

Standardized Pressure Levels (dbar)					
1	50	**15**	280	**29**	800
2	60	**16**	300	**30**	900
3	70	**17**	320	**31**	1000
4	80	**18**	340	**32**	1100
5	90	**19**	360	**33**	1200
6	100	**20**	380	**34**	1300
7	120	**21**	400	**35**	1400
8	140	**22**	450	**36**	1500
9	160	**23**	500	**37**	1600
10	180	**24**	550	**38**	1700
11	200	**25**	600	**39**	1800
12	220	**26**	650	**40**	1900
13	240	**27**	700	**41**	2000
14	260	**28**	750		

ESSDD
8, 509–566, 2015

Table 2. List of netCDF filenames where the mapped field variables for the different time composite periods are found.

Name of netCDF files
WeddellGyre_OM_Period2001to2013.nc
WeddellGyre_OM_Period2001to2005.nc
WeddellGyre_OM_Period2006to2009.nc
WeddellGyre_OM_Period2010to2013.nc

ESSDD
8, 509–566, 2015

Table 3. List of variable names in the accompanying netCDF file. The mapped variables listed are provided in the form of grids structured by latitude × longitude × pressure level, where fill values are NaNs. The asterisk (*) indicates variables which are not found in the netCdf file of the entire 11 year time period, *WeddellGyre_OM_Period2001to2013.nc*.

Variables provided in the netCDF files
Pressure Levels (dbar)
Latitude (DegN)
Longitude (DegE)
Tmax Conservative Temperature (DegC)
Tmax Absolute Salinity (gPERkg)
Tmax Pressure (dbar)
Tmax RHO (kgPERm3)
Tmax Conservative Temperature mapping error (DegC)
Tmax Absolute Salinity mapping error (gPERkg)
Tmax Pressure mapping error (dbar)
Tmax RHO mapping error (kgPERm3)
Conservative Temperature (DegC)
Absolute Salinity (gPERkg)
RHO (kgPERm3)
Conservative Temperature mapping error (DegC)
Absolute Salinity mapping error (gPERkg)
RHO mapping error (kgPERm3)
Tmax Conservative Temperature mask based on Period2002to2013
Tmax Absolute Salinity mask based on Period2002to2013
Conservative Temperature mask based on Period2002to2013
Absolute Salinity mask based on Period2002to2013
Tmax Conservative Temperature mask based on Period of file*
Tmax Absolute Salinity mask based on Period of file*
Conservative Temperature mask based on Period of file*
Absolute Salinity mask based on Period of file*

ESSDD
8, 509–566, 2015

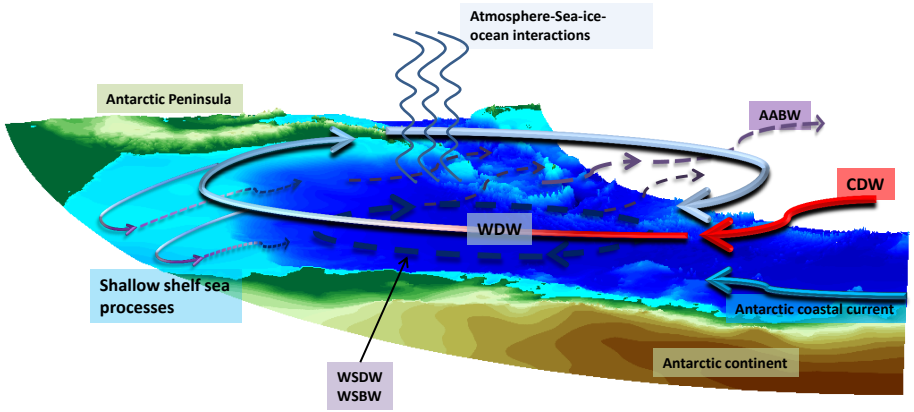

Figure 1. Schematic of Weddell Gyre circulation. The underlying 3-D map shows ocean bottom depth (GEBCO). Relatively warm Circumpolar Deep Water (CDW) enters from the east, becoming Warm Deep Water (WDW) which circulates in a cyclonic direction throughout the gyre, cooling on route, due to mixing with surrounding waters and interaction with the atmosphere and sea-ice processes. Shallow shelf sea processes leads to the formation of cold, high salinity water which, upon leaving the shelf, sinks below WDW to form Weddell Sea Deep and Bottom Water (WSDW and WSBW); WSDW exits the gyre to the north to become Antarctic Bottom Water (AABW).

ESSDD
8, 509–566, 2015

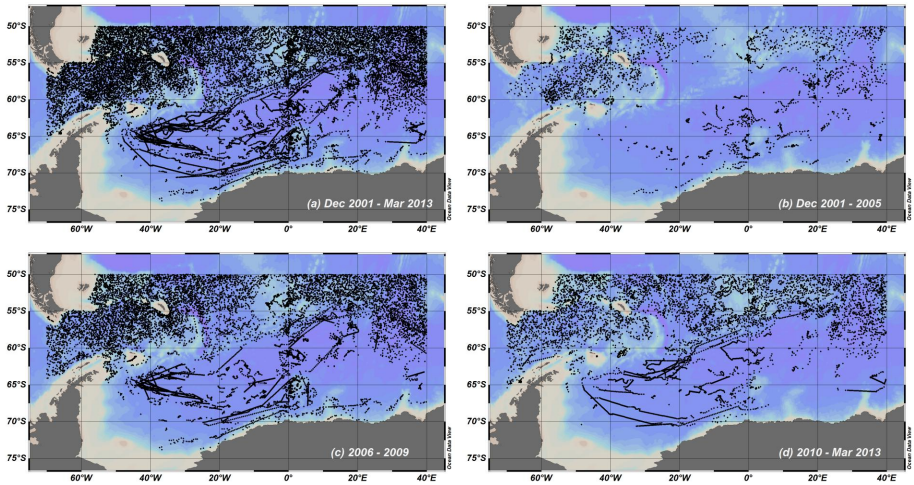

Figure 2. Argo float profile locations for **(a)** December 2001-March 2013; **(b)** 2002–2005; **(c)** 2006–2009 and **(d)** 2010–March 2013.

ESSDD
8, 509–566, 2015

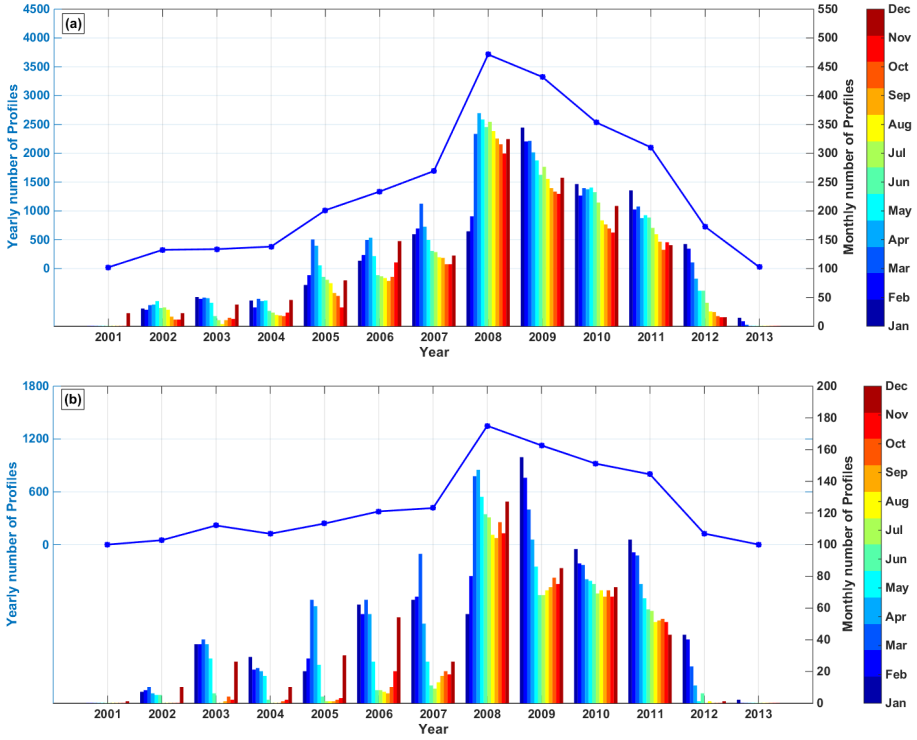

Figure 3. The number of profiles per year (line) and per month (bar) for **(a)** south of 50° S to the Antarctic continent and **(b)** south of 60° S to the Antarctic continent, between 70° W and 40° E.

ESSDD
8, 509–566, 2015

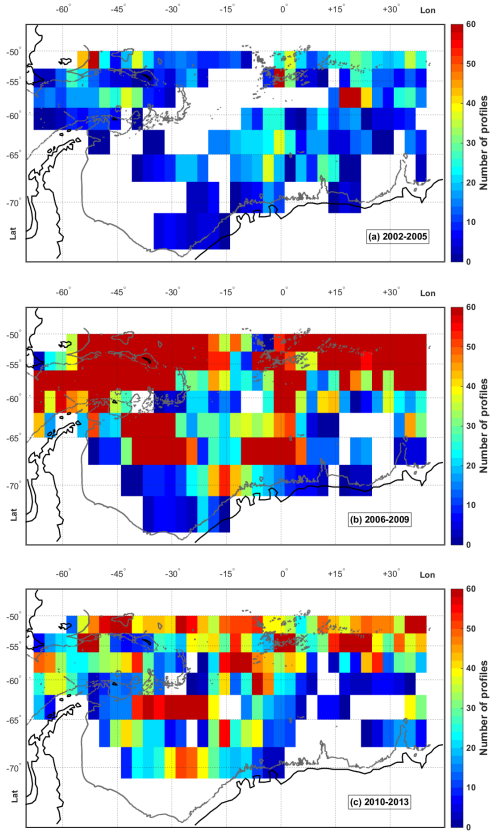

Figure 4. Argo float profile density (i.e. the number of profiles per 3° × 3° grid cell) for **(a)** 2002–2005; **(b)** 2006–2009 and **(c)** 2010–2013.

ESSDD
8, 509–566, 2015

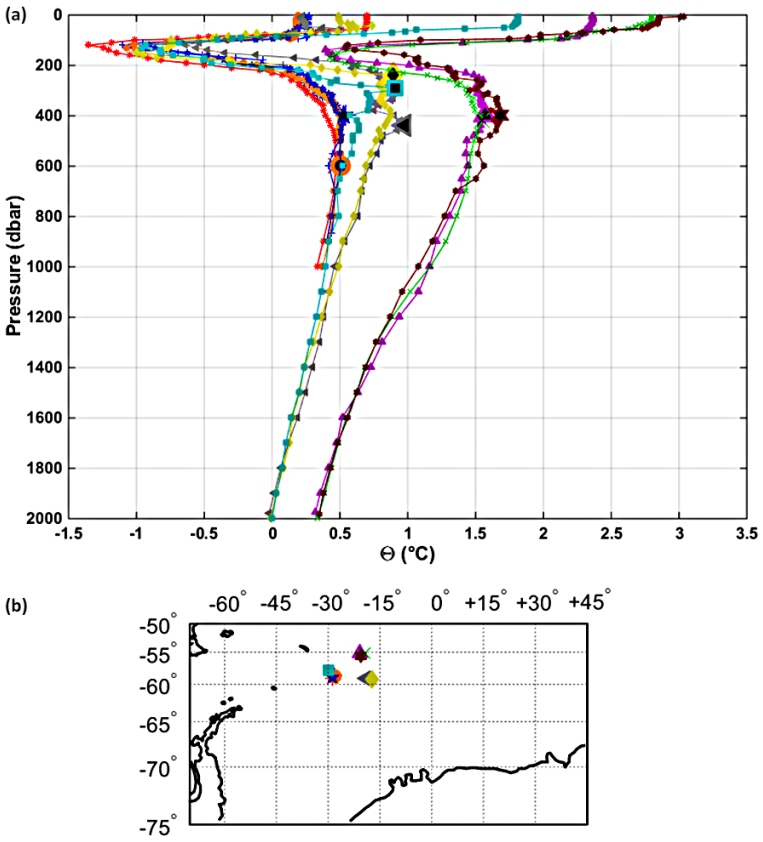

Figure 5. A random sample of pressure (dbar) – conservative temperature (°C) profiles from Argo floats within the region 15 to 30° W and 55 to 60° S **(a)** and the corresponding locations of the profiles **(b)**. The sub-surface temperature maximum of each profile is marked with an enlarged symbol.

ESSDD
8, 509–566, 2015

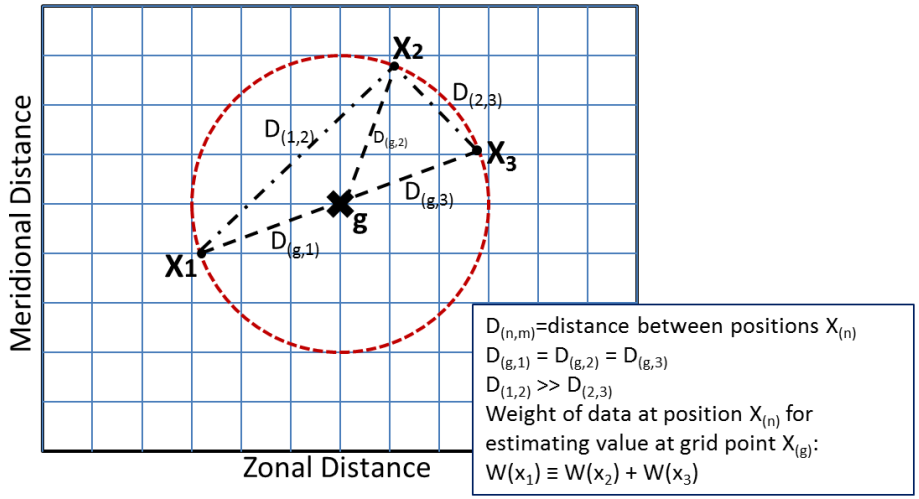

Figure 6. In objective mapping, the profile data are weighted based on their distance D to the grid point g, as well their distance to neighbouring profiles. Thus, while profiles x_1, x_2 and x_3 are all equally distanced from the grid point g, x_2 and x_3 are more closely spaced to each other than they are to x_1. Thus, the weight of x_1 would be equivalent to the sum of weights for x_2 and x_3 (i.e. $W(x_1) = W(x_2) + W(x_3)$).

ESSDD
8, 509–566, 2015

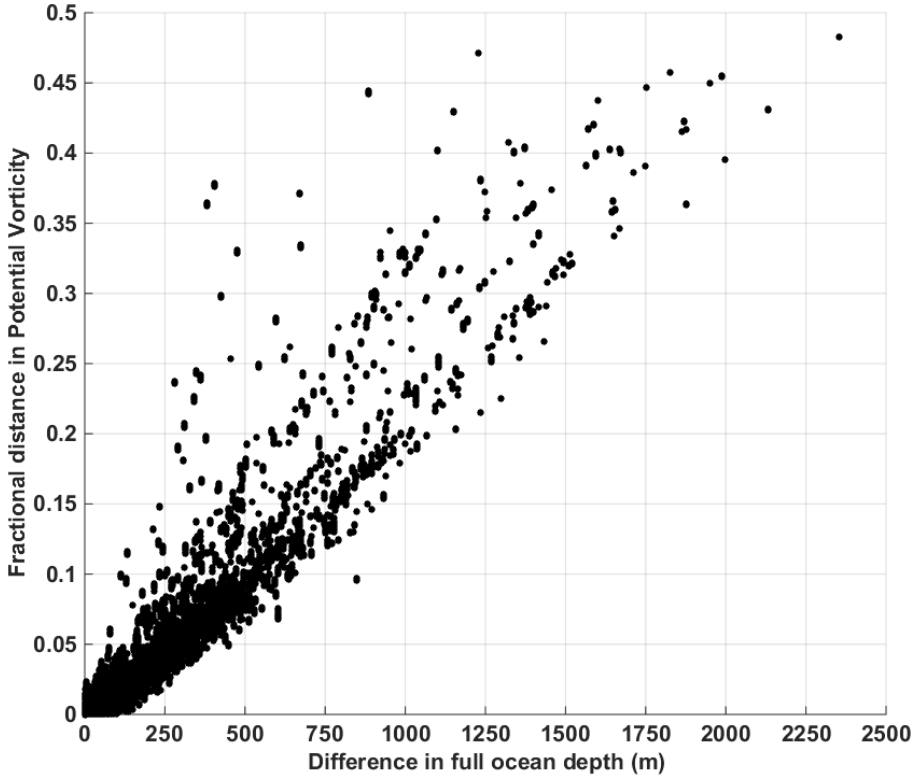

Figure 7. The fractional distance in potential vorticity (F) as a function of the difference in bottom ocean depth (H) between two locations. This is the generalised distance used in the decay scale of the covariance function in order to take into account cross-isobath separation (see text for explanation: Sect. 2.4).

ESSDD
8, 509–566, 2015

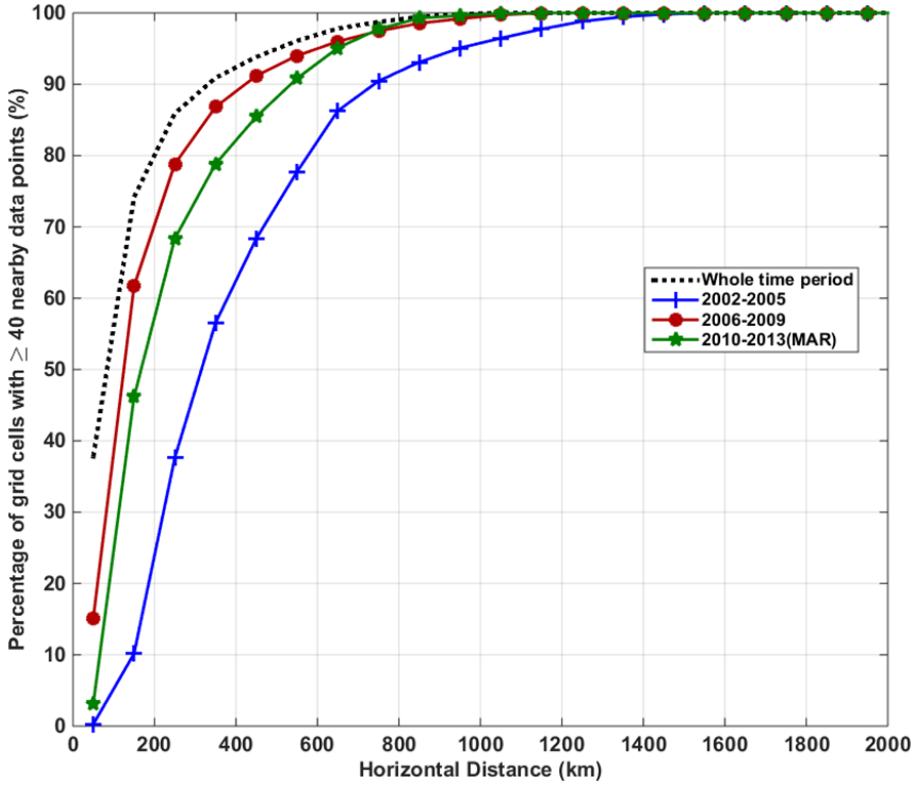

Figure 8. The percentage of grid cells with at least 40 profiles within an area of different radii, for different horizontal distances (km).

ESSDD
8, 509–566, 2015

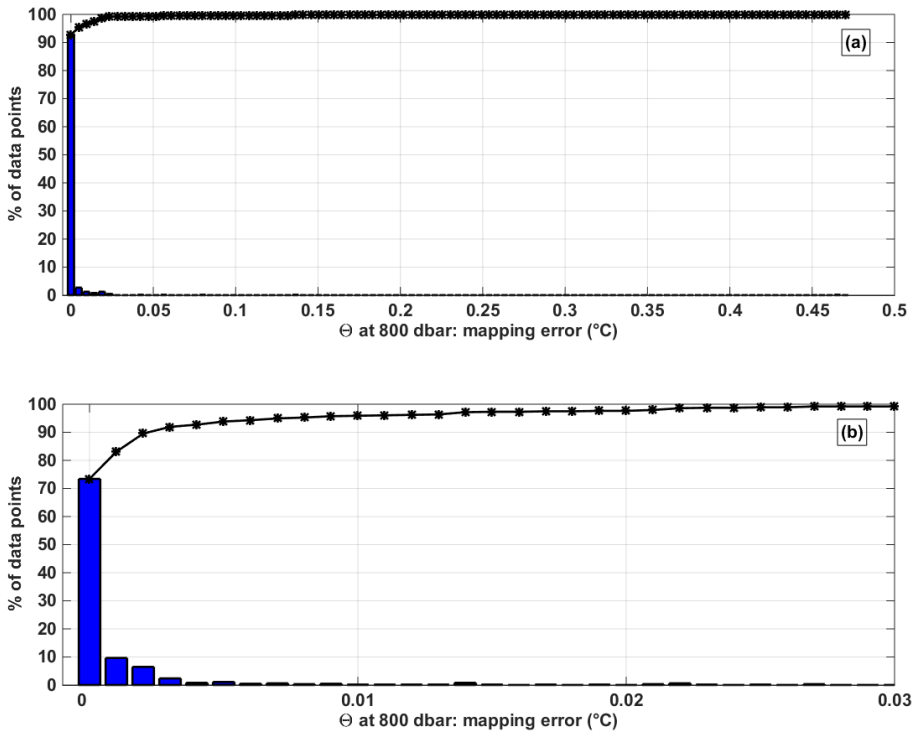

Figure 9. Conservative temperature (°C) at 800 dbar for 2002 to March 2013: histogram of the percentage of grid cells binned according to the mapping error variance (bar) and as a cumulative sum (line). **(b)** shows the same, zoomed in to lower error values.

ESSDD
8, 509–566, 2015

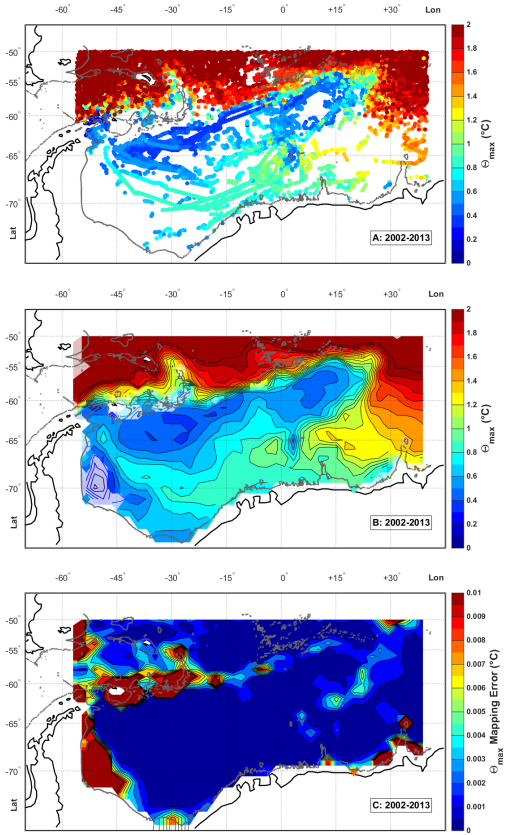

Figure 10. Conservative Temperature (°C) at the sub-surface temperature maximum for the entire time period from 2002 to 2013, where **(a)** shows the original float data, **(b)** shows the objectively mapped field and **(c)** shows the mapping error for the mapped field. The transparent regions in Fig. 10b mask regions where the mapping error is larger than the mapping error of 95 % of the grid cells (i.e. these regions fail the error mask criterion). For further information refer to Sect. 2.6. The error mask is applied to all contour plots of mapped variables.

ESSDD
8, 509–566, 2015

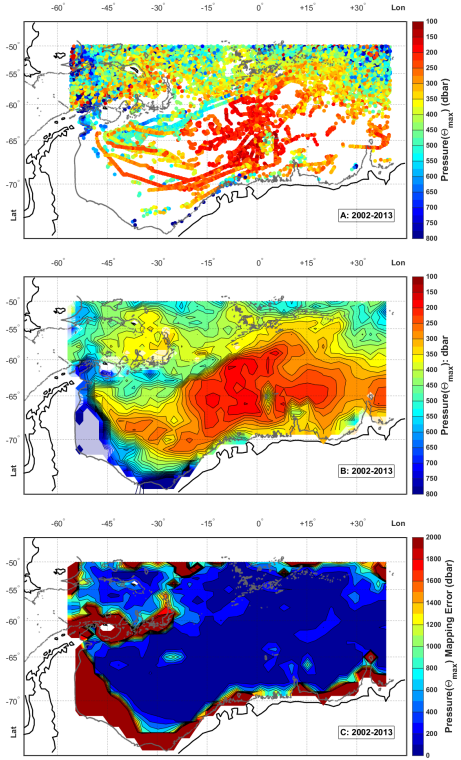

Figure 11. Pressure (dbar) at the sub-surface temperature maximum for the entire time period from 2002 to 2013, where **(a)** shows the original float data, **(b)** shows the objectively mapped field and **(c)** shows the mapping error for the mapped field. The transparent regions in Fig. 11b mask regions where the associated sub-surface temperature maximum mapping error is larger than the mapping error of 95 % of the grid cells (i.e. these regions fail the error mask criterion). For further information refer to Sect. 2.6. The error mask is applied to all contour plots of mapped variables.

ESSDD
8, 509–566, 2015

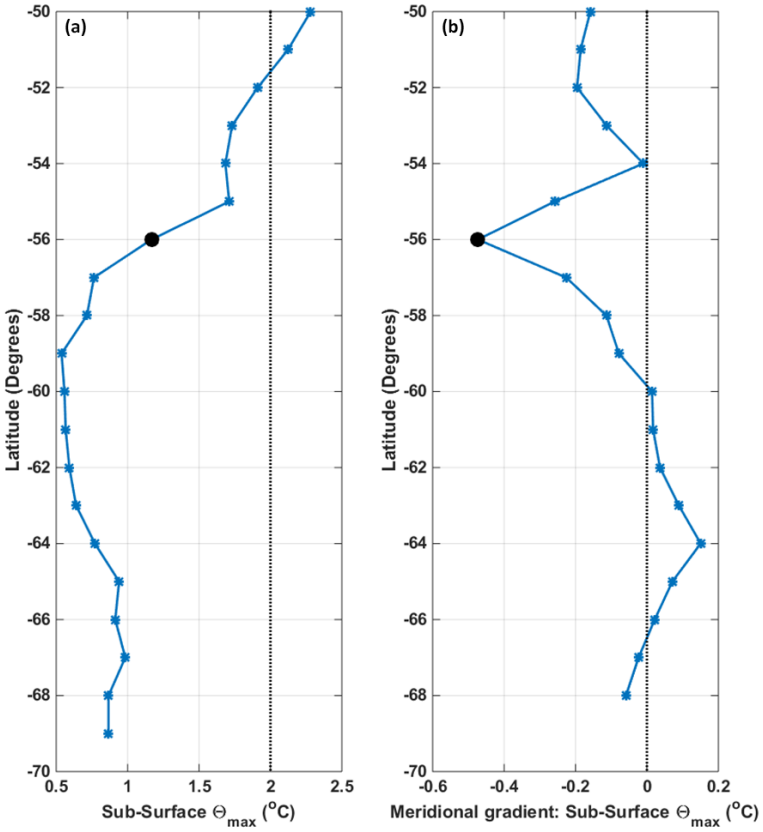

Figure 12. (a) Mean Meridional temperature distribution (°C) at the sub-surface temperature maximum extracted from the mapped field in Fig. 10b, for longitude bins encompassing the Prime Meridian. The meridional gradient of the temperature maximum is shown in **(b)**. The large, solid, circular symbols mark where the magnitude of the gradient is largest – this marks the latitude of the northern boundary of the gyre for this longitude.

ESSDD
8, 509–566, 2015

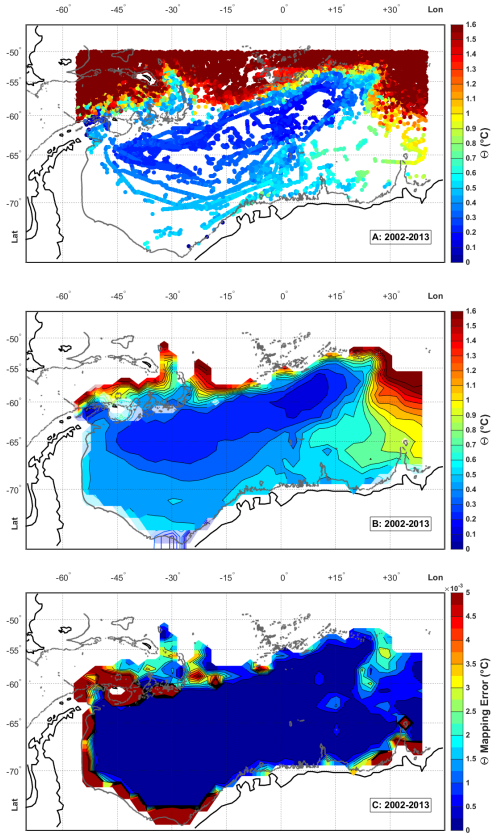

Figure 13. Conservative Temperature (˚C) at 800 dbar for the entire time period from 2002 to 2013, where **(a)** shows the original float data, **(b)** shows the objectively mapped field and **(c)** shows the mapping error for the mapped field. The transparent regions in Fig. 13b mask regions where the mapping error is larger than the mapping error of 95 % of the grid cells (i.e. these regions fail the error mask criterion). For further information refer to Sect. 2.6. The error mask is applied to all contour plots of mapped variables.

ESSDD
8, 509–566, 2015

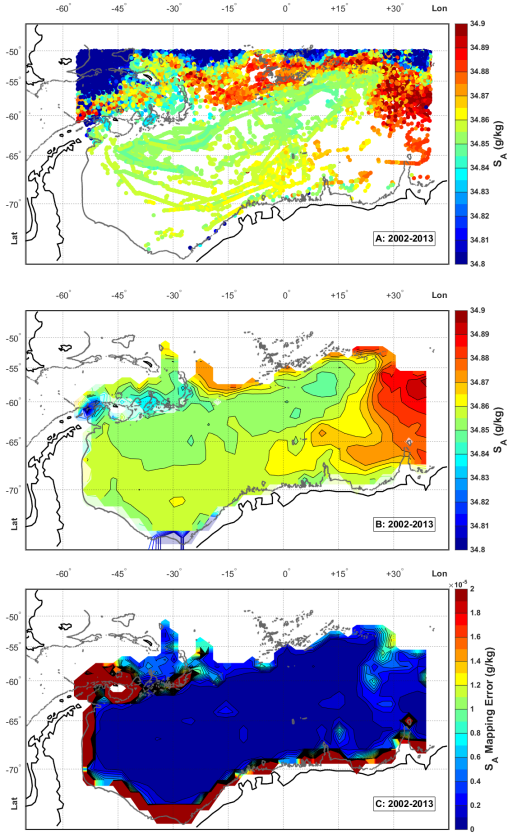

Figure 14. Absolute Salinity ($g\,Kg^{-1}$) at 800 dbar for the entire time period from 2002 to 2013, where **(a)** shows the original float data, **(b)** shows the objectively mapped field and **(c)** shows the mapping error for the mapped field. The transparent regions in Fig. 14b mask regions where the mapping error is larger than the mapping error of 95 % of the grid cells (i.e. these regions fail the error mask criterion). For further information refer to Sect. 2.6. The error mask is applied to all contour plots of mapped variables.

ESSDD
8, 509–566, 2015

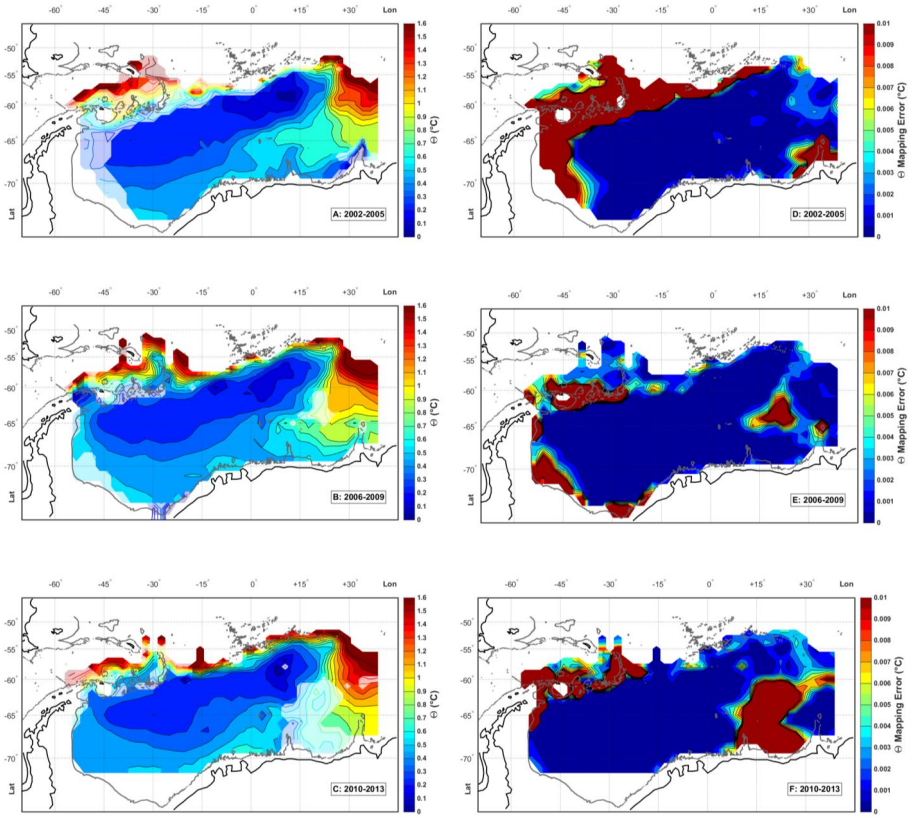

Figure 15. Conservative Temperature (°C) at 800 dbar for **(a)** 2002–2005; **(b)** 2005–2009 and **(c)** 2010–2013. The associated mapping errors for the corresponding time periods are shown in **(d–f)** respectively. The transparent regions in Fig. 15b mask regions where the mapping error is larger than the 2002–2013 mapping error of 95 % of the grid cells (i.e. these regions fail the error mask criterion). For further information refer to Sect. 2.6. The error mask is applied to all contour plots of mapped variables.

ESSDD
8, 509–566, 2015

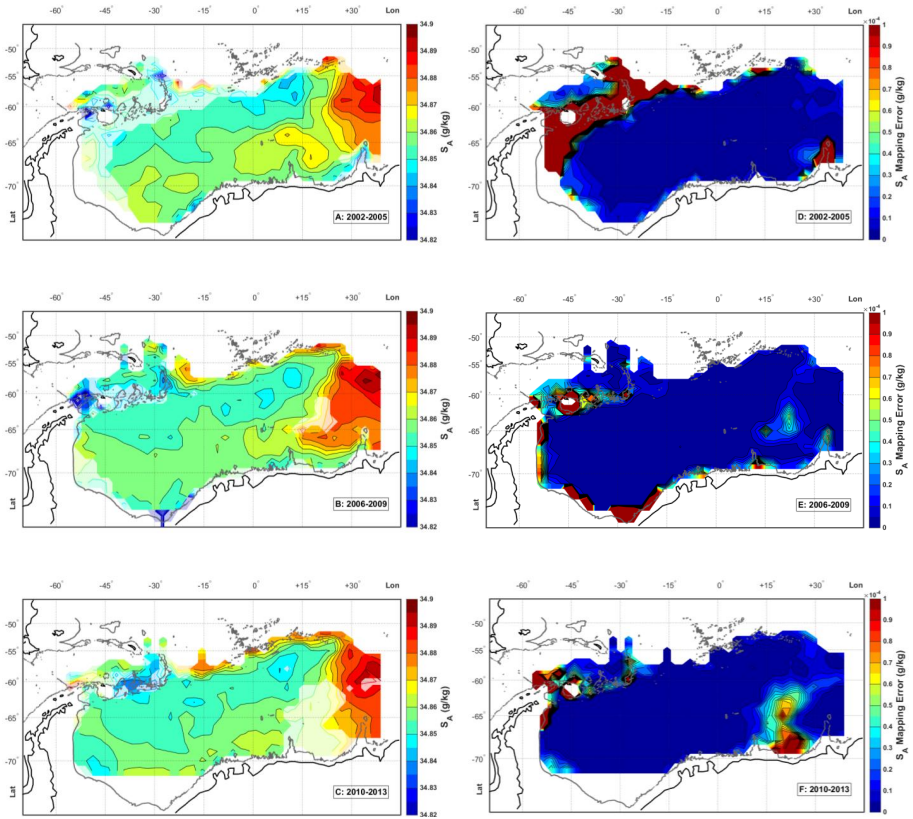

Figure 16. Absolute Salinity ($g\,kg^{-1}$) at 800 dbar for **(a)** 2002–2005; **(b)** 2005–2009 and **(c)** 2010–2013. The associated mapping errors for the corresponding time periods are shown in **(d–f)** respectively. The transparent regions in Fig. 15b mask regions where the mapping error is larger than the 2002–2013 mapping error of 95 % of the grid cells (i.e. these regions fail the error mask criterion). For further information refer to Sect. 2.6. The error mask is applied to all contour plots of mapped variables.

ESSDD
8, 509–566, 2015

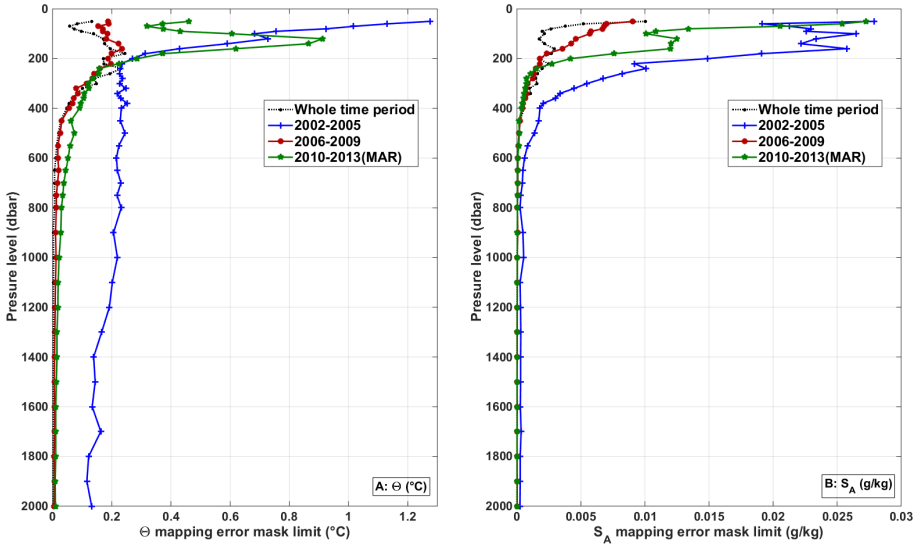

Figure 17. The vertical pressure profile of the 95 % error mask limits for **(a)** conservative temperature (°C) and **(b)** absolute salinity ($g\,kg^{-1}$) respectively; for the time periods 2002–2013 (black square), 2002–2005 (blue cross), 2006–2009 (red circle) and 2010–(March) 2013 (green star). The 95 % error limit denotes the value at which 95 % of all grid cells have smaller error variance (see Sect. 2.6 for full details).

ESSDD
8, 509–566, 2015

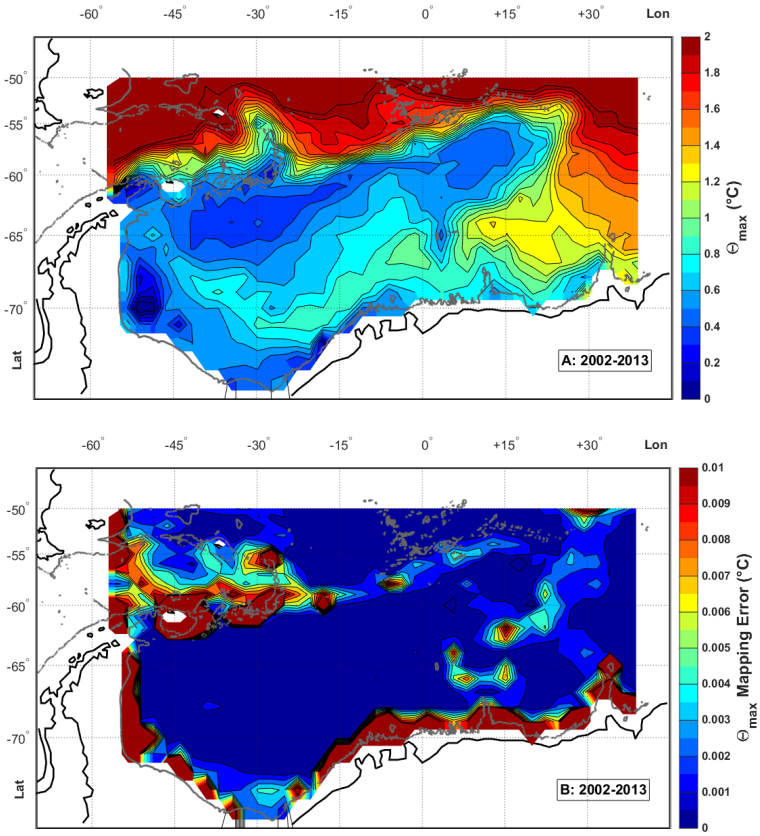

Figure 18. Conservative Temperature (°C) at the sub-surface temperature maximum for the entire time period from 2002 to 2013, where **(a)** shows the objectively mapped field based on the second approach (i.e. using the mapped pressure of the sub-surface temperature maximum to extract the temperature data points). The mapping error is shown in **(b)**. For more details, refer to Sect. 4.2.

ESSDD
8, 509–566, 2015

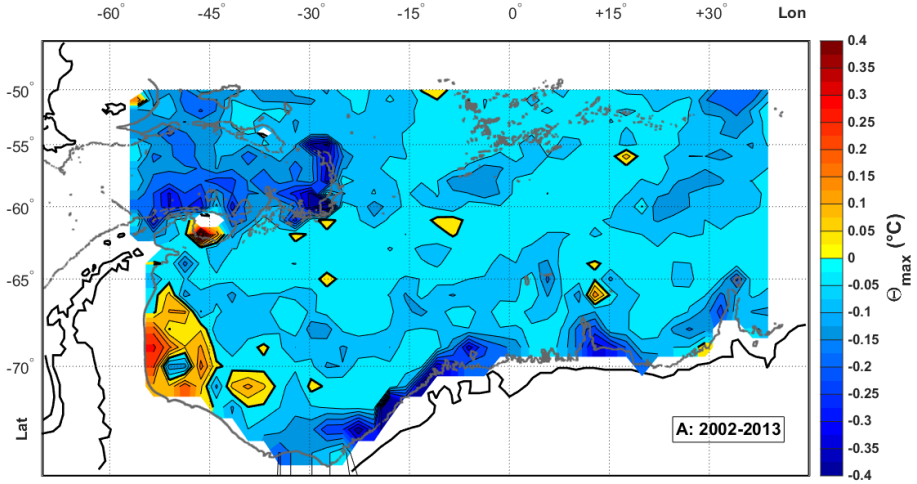

Figure 19. Comparing methods of mapping the sub-surface temperature maximum: this map shows the temperature difference (°C) where the output in the first approach in Fig. 10b is subtracted from the output of the second approach in Fig. 18a. Bold contour lines at 0 °C.

ESSDD
8, 509–566, 2015

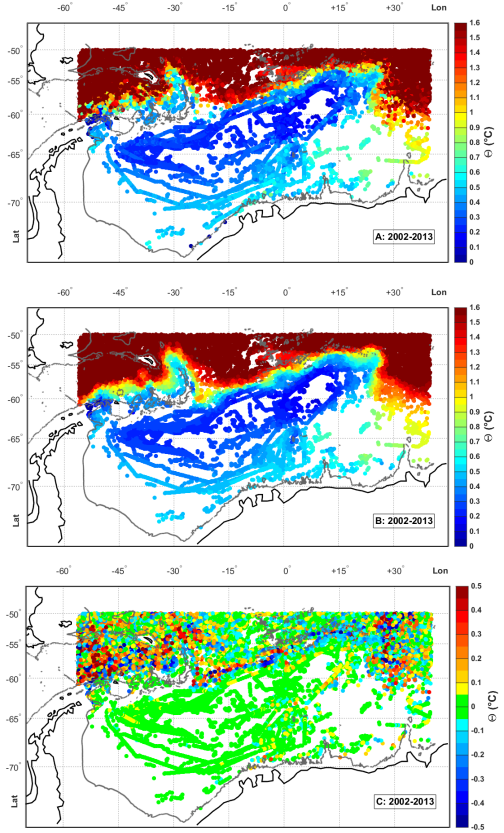

Figure 20. Conservative Temperature (°C) at 800 dbar for the entire time period from 2002 to 2013, where **(a)** shows the original float data, **(b)** shows the float data objectively mapped to the profile locations and **(c)** shows the difference where the output in **(b)** is subtracted from the original data in **(a)**.

ESSDD
8, 509–566, 2015

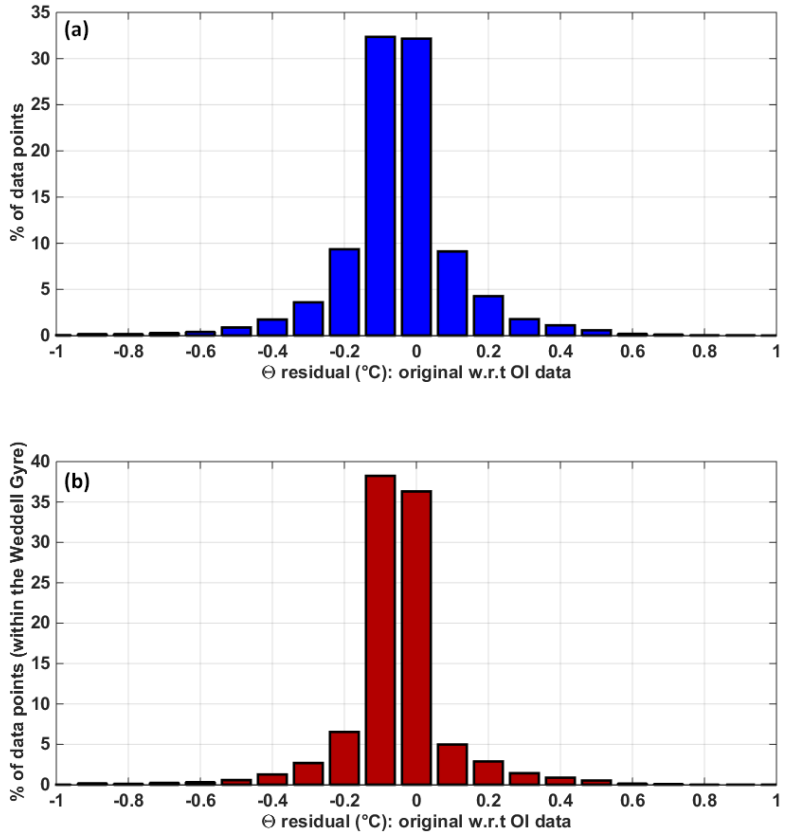

Figure 21. A histogram showing the percentage of data points binned by temperature residuals (°C) at 800 dbar, where the float data objectively mapped to the profile locations (i.e. Fig. 20b) are subtracted from the original profile data points (i.e. Fig. 20a), for **(a)** the entire dataset and **(b)** for those data points within the "defined" Weddell Gyre region only.

ESSDD
8, 509–566, 2015

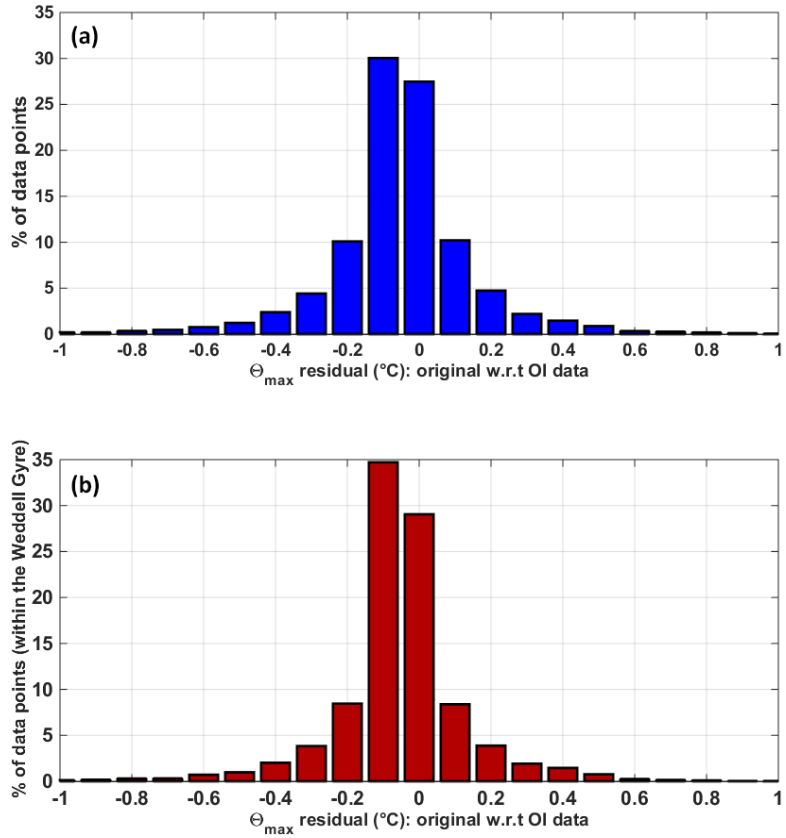

Figure 22. The percentage of data points binned by temperature residuals (°C) at the subsurface temperature maximum, where the float data objectively mapped to the profile locations are subtracted from the original profile data points, for **(a)** the entire dataset and **(b)** for those data points within the "defined" Weddell Gyre region only.

ESSDD
8, 509–566, 2015

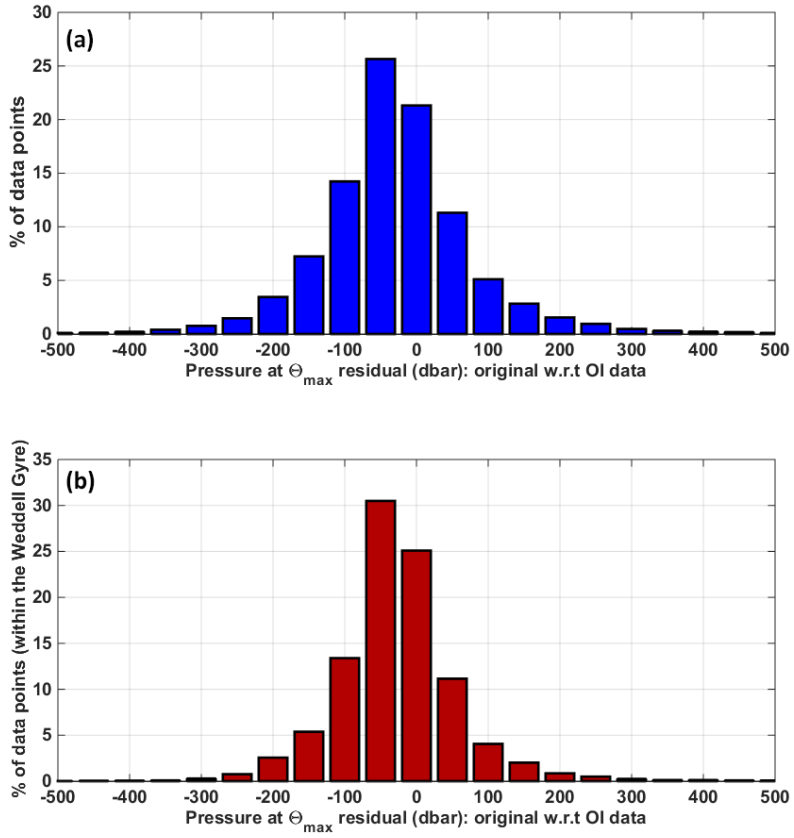

Figure 23. The percentage of data points binned by pressure residuals (dbar) at the level of the sub-surface temperature maximum, where the float data objectively mapped to the profile locations are subtracted from the original profile data points, for **(a)** the entire dataset and **(b)** for those data points within the "defined" Weddell Gyre region only.

ESSDD
8, 509–566, 2015